TÉCNICO LISBOA

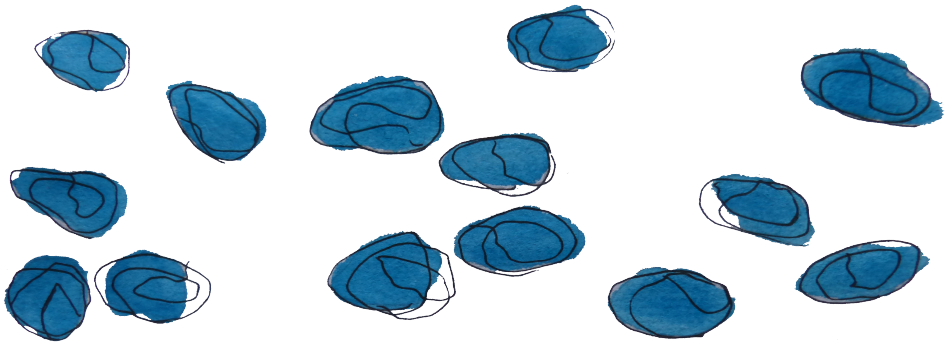

Describing monolayer mechanoresponse from nuclear morphology and dynamics: a computational approach

Maria Teresa Bento Parreira

Thesis to obtain the Master of Science Degree in

Biomedical Engineering

Supervisors: Prof. Kris Noel Dahl
Prof. João Miguel Raposo Sanches

Examination Committee

Chairperson: Prof. Cláudia Alexandra Martins Lobato da Silva
Supervisor: Prof. Kris Noel Dahl
Members of the Committee: Prof. Susana de Almeida Mendes Vinga Martins
Dr. Elsa Logarinho

January 2021

I declare that this document is an original work of my own authorship and that it fulfills all the requirements of the Code of Conduct and Good Practices of the Universidade de Lisboa.

Preface

The work presented in this thesis was performed at Instituto de Sistemas e Robótica, Instituto Superior Técnico (Lisboa,Portugal), during the period February-December/2020, under the supervision of Prof. Kris Dahl at Carnegie Mellon University. The thesis was co-supervised at Instituto Superior Técnico by Prof. João Sanches.

The preparation and imaging of the biological data used for the present analysis were skillfully carried out by Kirill Lavrenyuk in the Dahl Lab for Subcellular Structure and Engineering, Department of Chemical Engineering, at Carnegie Mellon University, Doherty Hall.

Acknowledgments

Full of hopes and expectations, prepared to do my best and eager to learn more. I find myself, at the present moment, experiencing a similar feeling to when I first stepped into Instituto Superior Técnico as a student of Biomedical Engineering. Yet, who I was then and who I've become don't coincide: we are separated by five years of numerous lessons, unbelievable growth and wonderful memories. Another thesis-long document could be written about the adventures, and the people, which made up this journey. I am overwhelmed with gratitude for all the opportunities I was given and I can only hope I have made the best (my best) out of them all.

First, I would like to thank Professor João Sanches and Professor Kris Dahl, for their availability, valuable advice and for believing in my work enough to both send me across the seas and be willing to take me in when I arrive. I also want to thank Kirill Lavrenyuk, for his work at the lab and for answering all my questions regarding this new world of academic research.

Then, the colleagues who became friends. Thank you. From the first class, for making me feel less alone for not knowing what a matrix was, to the shared procrastination of getting the thesis done. The people I met have taught and inspired me more than I realise and I cherish every late night, either working or toasting to new challenges.

Thank you to all the friends I kept from home. To José Esteves, who was never able to finish his own journey but who became a crucial part of ours.

And, finally, thank you to my family, whose incessant stream of support has me at a loss for words. You believe in me more than I believe in myself and my definition of success is built on the idea of being able to give back some of the joy and opportunities you have provided for me. To my uncles and aunts, to my mother, father, and to my sister, whose future accomplishments I cannot wait to applaud.

Abstract

Cells exhibit complex behaviour in response to mechanical stimuli, which is not yet fully understood. Studying how cells with defective mechanotransduction affect their neighbours and how this response propagates within a monolayer can help shed light on mechanisms of cellular stability and cell-cell interactions, with an impact on the study of diseases such as laminopathies or cell invasion during cancer.

Here, NRK-52E cells transfected with lamin A Del50, which significantly stiffens the nucleus, were sparsely placed in a monolayer of normal, non-expressing NRK-52E cells. Through morphometric analysis and tracking, the nuclei, which play a pivotal role in mechanoresponse, were characterized and compared to a control monolayer. A method for a detailed analysis of the spatial aspect and temporal progression of the nuclear boundary was developed and used to achieve a full description of the phenotype and dynamics of the monolayers under study.

Our findings reveal that cells are highly sensitive to the presence of mechanically impaired neighbours, leading to generalized loss of coordination in collective cell migration and significant changes in nuclear morphology, but without seemingly affecting the dynamics of nuclear lamina fluctuations of non-expressing cells. Interestingly, some characteristics of the behaviour of these cells appear to be dependent on the distance to a mutant cell, pointing to compensatory behaviour in response to force transmission imbalances in a monolayer.

Keywords

bioimage analysis; mechanotransduction; nuclear morphometry; monolayer dynamics; HGPS.

Resumo

As células exibem respostas complexas a estímulos mecânicos, que ainda não são completamente compreendidas. Descrever a forma como células com mecanotransdução deficiente podem afetar células vizinhas, e como este efeito se propaga numa monocamada celular, pode elucidar sobre mecanismos de estabilidade celular e interações célula-célula, com impacto no estudo de condições como laminopatias ou invasão em cancro.

Aqui, células NRK-52E transfectadas com lamin A Del50, cujo efeito inclui o aumento da rigidez nuclear, foram colocadas numa monocamada de células NRK-52E normais, não transfectadas. Através de análise morfométrica e rastreamento, os núcleos, que possuem um papel central na resposta a estímulos mecânicos, são caracterizados e comparados com os de uma monocamada controlo. Foi desenvolvido um método que permite uma análise detalhada do aspeto espacial e progressão temporal do contorno nuclear, utilizado para a obtenção de uma descrição completa do fenótipo e dinâmica das monocamadas sob estudo.

Os resultados da análise revelam que as células são extremamente sensíveis à presença de vizinhos com resposta mecânica comprometida, provocando uma perda de coordenação generalizada na migração celular e a diferenças significativas na morfologia nuclear, sem no entanto parecer afetar a dinâmica das flutuações da membrana nuclear. Curiosamente, foram observados efeitos dependentes da distância a uma célula comprometida, indiciando um comportamento compensatório que pretenderá dar resposta a defeitos mecânicos numa monocamada em equilíbrio.

Palavras Chave

análise de bioimagens; mecanotransdução; morfometria nuclear; dinâmica de monocamadas; HGPS.

Contents

List of Figures

List of Tables

Acronyms

2D	two-dimensional
3D	three-dimensional
AC	Active Contours
AFM	Atomic Force Microscopy
C	Control
CI	Confidence Interval
CV	Coefficient of Variation
DMEM	Dulbecco's Modified Eagle Medium
ECM	Extracellular Matrix
FBS	Fetal Bovine Serum
FD	Focal Distance
FOV	Field-of-View
HGPS	Hutchinson-Gilford Progeria Syndrome
HK-means	Hierarchical K-means
LBPs	Lamin Binding Proteins
LINC	Linker of Nucleoskeleton and Cytoskeleton
M	Mutant
MSD	Mean Square Displacement
MSE	Mean Squared Error
NA	Numerical Aperture
NE	Non-expressing
NRK-52E	Normal Rat Kidney Epithelial

PBS	Phosphate Buffered Saline
PC	Principal Component
PCA	Principal Component Analysis
ROI	Region of Interest
SNR	Signal-to-Noise Ratio
SURF	Speeded-Up Robust Features
TAN	Transmembrane Actin-associated Nuclear
WT	Wild Type

1

Introduction

Contents

1.1 Motivation

Basic and clinical research based on imaging has allowed for the study of numerous biological processes. Computational processing of this data has lead to remarkable advances, as it often allows for the extraction of relevant features, making use of effective and more objective methods [1]. As imaging technology improves and techniques for better manipulation of biological material are developed, the volume of data easily acquired for a study increases. This might contribute to statistical robustness of observations, but demands a method of analysis that can encompass large data inputs and produce significant results.

Numerical-based feature extraction can provide large data amounts at low computational expenses. Data preprocessing, involving the segmentation of cells or nuclei and appropriate tracking, emerges as a bottleneck step [2]. However, intensity patches of the Region of Interest (ROI)s and respective coordinates over time constitute a database with light storage demands but numerous analysis possibilities. Because morphology is so closely related to function in numerous cellular mechanisms [3], an objective, quantitative description of such features can give insight into mechanisms or effects of observable phenomena, as well as reveal new phenomena which cannot be easily captured by manual analysis.

In the field of cellular research, a large array of computational methods can be applied towards achieving a more complete and objective characterization of the architecture and flow of a monolayer of cells. Complex mechanisms modulate cellular stability and structure, but the mechanical balance of a monolayer can be easily affected by the presence of disrupting factors such as abnormally responsive cells [4]. Those changes in behaviour are at the origin of pathological phenomena such as cellular extrusion upon metastasis [5], involving force transmission imbalances within the tissues.

Laminopathies are yet another example of how impaired mechanoresponse can have serious consequences in the viability of tissues [6] as well as life expectancy [7]. These are diseases in which the stiffness of the nucleus may be out of the physiological range. This subcellular component plays a pivotal role as a mechanosensor [8] and it is largely responsible for modelling cellular response to mechanical changes in the environment, but many questions remains unanswered regarding the mechanisms by which cells sense and adjust to their surroundings. How can one defective cell affect monolayer dynamics and force transmission? And, if such effects are observed, what is the range of impact? Learning the answers to these questions can boost the understanding on cellular homeostasis and disease progression.

Nuclear mechanoresponse can involve shape deformation and variation of relative position in the cell [9]. Furthermore, because the nucleus is intimately related to efficiency of cell migration [10], relating morphological alterations with nuclear motion can shed light on the mechanisms affected by abnormal mechanosensing and response; consequently, studying mechanotransduction mechanisms can involve characterizing nuclear phenotype and motion.

1.2 Original contributions

The characterization of nuclei from cells with Hutchinson-Gilford Progeria Syndrome (HGPS), a laminopathy where the nucleus is stiffer, has been widely described [11–13]. Nonetheless, it is yet unclear how the presence of a mechanical impaired cell - where a mutation is affecting nuclear stiffness - can affect the behaviour of its healthy neighbours.

This work analyses the nuclear phenotype, morphology dynamics and nuclear motion in a monolayer of normal Normal Rat Kidney Epithelial (NRK-52E) cells, with a roughly estimated density of 10% of NRK-52E cells which have been transfected with lamin A Del50 (a mutation responsible for the HGPS, causing the nucleus to stiffen). We seek to determine if and how the presence of these Mutant (M) cells affects monolayer dynamics by comparing observations to a control condition, a monolayer containing only normal, Wild Type (WT) NRK-52E cells. This analysis is achieved using a high-throughput methodology, with minimal human intervention. A detailed characterization of nuclear edge shape and dynamics is conceptualized and developed, and these results are crossed with features from monolayer dynamics. We also investigate whether distance to an M cell affects nuclear behaviour.

The conceptualization of new features to assess spatial progression of the nuclear boundary - a proxy for its shape and roughness - as well as its temporal progression - how the boundary is changing over time, unveiling a detailed quantification of nuclear membrane fluctuations - becomes an important tool towards nuclear and cellular characterization, with many potential applications. As such, a complete portrait of nuclei behaviour is accomplished here, unveiling mechanisms of cell-cell interactions and response to mechanical stimuli, with implications on the study of disease progression and modelling.

The main findings in this work are to be submitted for publication soon [14].

1.3 Thesis Outline

The present dissertation is organized as follows: first, in Chapter 2, a brief introduction on the current knowledge on mechanotransduction mechanisms, related pathologies and implications is presented, as well as a brief review of the state-of-the-art of computational methods of analysis of fluorescent microscopy images. Chapter 3 describes the methodology and techniques used for data acquisition and processing, specifying the different sets of features calculated and what information can be extracted. Next, Chapter 4 presents all the significant findings, correlating them with the biological processes underlying the conditions under study. Finally, in Chapter 5, a summary of the findings and suggestions on future directions of related research are presented.

2

Background and related work

Contents

2.1 Mechanotransduction

Cells are highly sensitive to their physical environment. The mechanisms by which they adapt to mechanical stimuli, such as extracellular forces exerted by neighbouring cells or intracellular forces stemming from responses to substrate or Extracellular Matrix (ECM) stiffness, are part of a process called mechanotransduction [8]. The mechanosensitive feedback which is generated is responsible for modulating vital cellular functions such as proliferation and differentiation, migration and apoptosis [15].

Mechanical stimuli in an epithelial monolayer can be propagated through the activity of myosin proteins, cell-cell adhesion and cytoskeletal remodelling [16]. The nucleus, however, is at the center of cellular response to mechanical changes in the environment and it is often seen as a mechanosensor of high importance for normal cell behaviour [8]. Understanding how this component senses and adjusts to physical cues begins with understanding its architecture and how it interacts with the remaining structural elements of the cell.

2.1.1 Nuclear Structure

The nucleus, in eukaryotic cells, is generally the largest and stiffest organelle, where the genome is contained and transcription takes place. This organelle is composed of two regions, nuclear envelope and nuclear interior, whose structure and function differ [8]. The nuclear interior includes the DNA, binded to histones and organized into dynamic chromatin structures which can be more or less condensed during the cell cycle, as well as several other nuclear elements such as Cajal bodies or structural proteins. Conversely, the nuclear envelope includes a well-defined double-membrane (two phospholipid bilayers, inner and outer membrane, where nuclear pores allow for molecular transport) and the nuclear lamina, a dense network of proteins underlying the inner nuclear membrane.

The nuclear lamina is mainly composed of the lamins, which can also form structures in the nuclear interior. Lamins are type V intermediate filament proteins which can determine nuclear morphology but whose functions range from regulation of DNA replication and repair [17] to nuclear positioning and mechanosensing [9]. They can be divided into subtypes A (lamins A and C, which result from the alternative splicing of the LMNA gene) and B (LMNB1 and LMNB2 genes).

Lamins of subtype B are expressed in adult animals and in all cells during development [8]. While B-type lamins can increase nuclear rigidity, they seem to have less influence in determining nuclear stiffness when compared to A-type lamins [18]. In contrast, lamins of subtype A are found in the majority of differentiated cells and regulate nuclear shape, structure and stability [19]. They have been reported to also influence gene expression through mechanisms which involve chromatin [20], since the nuclear lamina binds to heretochromatin via Lamin Binding Proteins (LBPs).

This element has been shown to be essential for maturation and cellular survival under mechanical

stress [9]. In fact, by modulating nuclear stiffness, the lamina contributes significantly to the structural integrity of a nucleus [8]. Interestingly, nuclear rheology can be modelled using a spring-dashpot circuit, where lamin A/C are responsible for viscosity and B-type lamins generate elastic responses to stretching [21].

2.1.2 Nuclear-cytoskeleton coupling

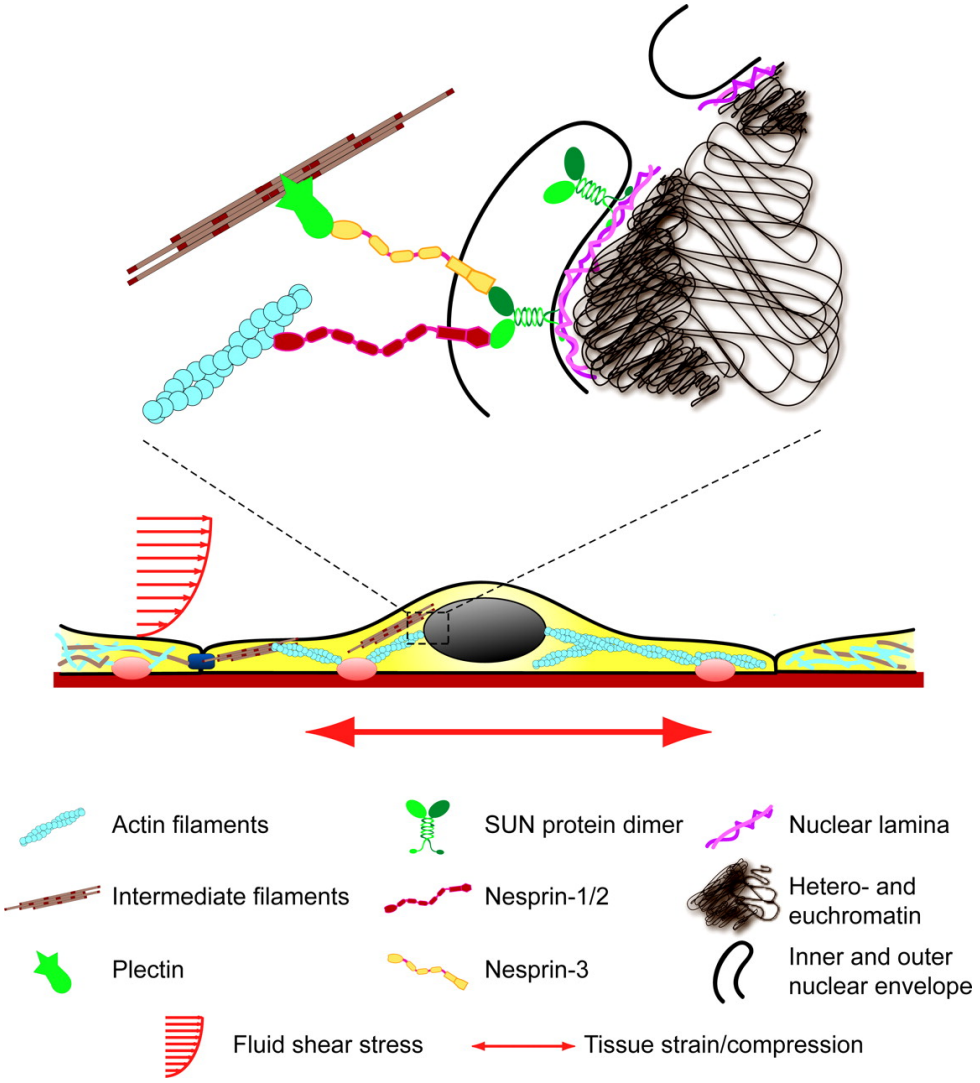

Figure 2.1: Pathways of force transmission from the extracellular matrix to the nucleus. Retrieved from [8]. Plectin, a cross-linker, can interconnect actin filaments, intermediate filaments, and microtubules and binds to nesprin-3, while nesprin-1/2 binds to actin filaments. SUN proteins connect nesprins to the nuclear envelope, via lamins, which in their turn bind to chromatin and DNA. External forces, such as substrate strain or fluid shear stress, can then be transmitted to the nuclear interior.

The cytoskeleton is a complex heterogeneous structure which consists mainly of three elements: actin microfilaments, microtubules and intermediate filaments. These components provide support to the cell, allowing for protein and organelle movement, influence cell shape and play an important role in mechanical stability [8]. When force is transmitted to the cell, the components of the cytoskeleton reorganize and compensate for this stimulus.

A-type lamins are involved in nuclear-cytoskeletal coupling and mechanical stress transmission through the Linker of Nucleoskeleton and Cytoskeleton (LINC) complex [22]. Lamins in the inner nuclear membrane are connected to SUN (SUN1 and SUN2) proteins. These proteins connect with Nesprin1 and Nesprin2, which bind to F-actin at the outer nuclear membrane, or to Nesprin3, which binds, via plectin, to intermediate filaments [22], thus creating a physical connection between the nuclear interior and the cytoskeleton. Figure 2.1 illustrates briefly which elements are involved and how they interact. Due to the role of lamins in nuclear integrity and morphology, force transmission to the nuclear interior via lamin-cytoskeleton coupling can induce the deformation of the nucleus [19].

This deformation is essential for cell survival in response to mechanical stress, but proper flexibility of the nuclear envelope and adequate nucleus-cytoskeleton coupling also come into play during cell motion.

2.1.3 The role of the nucleus in collective cell migration

A large number of physiological processes are dependent on the ability of cells to move within their environment. Cell migration plays an important role in tissue development and repair, but it can also be impacted in pathological conditions such as cancer [23].

Upon cell migration, the cytoskeleton and the nucleus adjust their structure and positioning, allowing for the establishment of cell polarity. More specifically, nuclear positioning is the result of a dynamic interaction between the cytoskeleton and the LINC complex which is influenced by the process of mechanosensing in cell-cell junctions (which connect cells to eachother in a monolayer) and focal adhesions (which connect cells to the ECM) [23].

During collective cell migration, the nucleus is usually positioned in the back of the cell, a rearward movement caused by an actin retrograde flow. Transmembrane Actin-associated Nuclear (TAN) lines are composed of LINC complex proteins and actin filaments and allow this movement to occur by connecting the lamina to the actin filaments [23]. Other elements of the cytoskeleton may also come into play, as both microtubules and intermediate filaments have been associated with nuclear translocation and rotation [24].

Perturbations to nuclear integrity and structural coupling have clear implications in a cell's ability to move [24]. However, in spite of important findings regarding the internal organization and interaction of cell components, the mechanisms of nuclear positioning during cell motion are not yet entirely under-

stood.

Collective cell migration is driven by active forces generated within each cell, as described above, but many extra factors come into play, namely neighbour cells' deformability and polarization and cell-cell adhesion and signaling [25]. Force transmission between adjacent cells occurs at cell-cell junctions, which link to actomyosin within each cell [26], creating cohesion energy and surface tension in a monolayer. Due to cytoskeleton elasticity, cell-cell repulsion also occurs and an efficient collective migration requires these forces to be balanced. More details on force balance in a monolayer can be seen in Figure 2.2 which, in a simplified scheme, illustrates the wide range of forces and cellular structures involved in a monolayer in equilibrium. Because the cellular interior is tightly connected with its exterior, mechanical changes in either cell components or in the substrate or neighbouring cells will influence cellular response and ability to migrate.

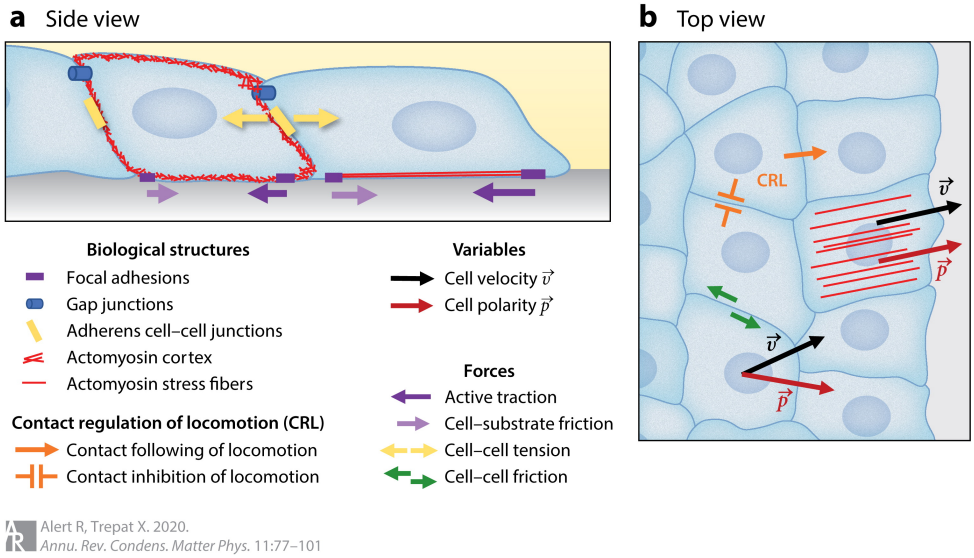

Figure 2.2: Schematic representation of the forces and interactions of migrating cells in an epithelial monolayer, retrieved from [26]. Internal force generation and transmission is dependent on cell-cell and cell-substrate interactions. Biological structures involved are illustrated, as well as some of the forces which are commonly involved in migratory equilibrium. Variables used to characterize cell motion are also included.

Nuclear elasticity has been shown to influence migration speed, with higher nuclear stiffness being associated with smaller migration rates [10]. Because lamins A/C are coupled with structural elements of the cell, disturbances in their distribution lead to a defective functional organization of the cytoskeleton, which affects cell dynamics. In fact, LmnA -/- cells have decreased migration speed as a consequence of decreased cell contractility [27]. Deformability of the nucleus, which has been mentioned to be regulated by lamins, has also been found to be a rate-limiting feature for migration [18].

Interestingly, Graham et al. [27] describes the nucleus as a non-essencial component for two-dimensional (2D) migration and cell polarization; however, their findings reveal that regulation of cell contractility and

the activation of mechanosensitivity pathways are dependent on this element of the cell.

2.1.4 Laminopathies

The important role of the nuclear lamina in mechanotransduction, nuclear shape and migration has been described above. Mutations in the LMNA gene (which codes for lamins A and C) are called laminopathies. These diseases include several forms of muscular dystrophy, such as Emery-Dreifuss or limb girdle muscular dystrophy, dilated cardiomyopathy or Hutchinson Gilford progeria syndrome, discussed below.

The specific molecular mechanisms through which some of these diseases take effect are still not fully known [8], but nuclear mechanosensing, morphology, stiffness and fragility appear to be affected [6]. Actin cytoskeletal organization, which is involved in cellular mechanoresponse and migration, has also been shown to be affected in laminopathies, with significant consequences in cell functioning. Moreover, the disruption of the levels of lamin-A is strongly related to several other human diseases. The stiffness of a tissue has been shown to scale with the levels of lamin-A [17], but abnormaly lower or higher levels of lamin-A have been correlated with cancerous cells [28].

A nucleotide substitution (GGC to GGT) is the most frequently reported cause of HGPS, which leads to the deletion of 50 amino acids near the C-terminus of the lamin A molecule, often designated lamin A Del50 or progerin [7]. HGPS cells have increased levels of lamin A near the nuclear envelope, which results in nuclei that are stiffer [11]. Patient cells are characterized by defects in nuclear structure and morphology, with HGPS cells often displaying lobulated nuclei [29], even upon introduction of lamin A Del50 into normal cells by transfection [11]. These cells usually have higher values of circularity [4, 12], due to inability to properly elongate, but exhibit a more concave morphology due to the presence of micro-dysmorphic shapes [13]. These differences in nuclear shape could be associated with changes in lamin organization [4].

Further morphological and mechanosensing differences may be attributed to the impact of the mutation on mechanical properties of the nucleus, which are conveyed by chromatin arrangement and structure [30]. Because lamins A/C bind to chromatin, they can be linked to chromatin organization, transcription regulation and DNA repair [7].

HGPS cells have been shown to have impaired migration, with increased nuclear defects as a consequence of attempting to migrate through small spaces [13]. This reduced cell motility could result from increased nuclear resistance and decreased actin-myosin force generation. Due to the previously mentioned decrease in nuclear deformability, three-dimensional (3D) cell migration is significantly affected, and 2D traction force is also reduced. Additionally, HGPS affects the establishment of cell polarity [31], since rearward nuclear movement, typical during cell migration, is inhibited in these cells. This could be attributed to the overaccumulation of SUN1 proteins – proteins which are a part of the LINC complex -,

which induces excessive association of microtubules with the nucleus and causes polarity defects [32].

Philip and Dahl [4] demonstrated that both normal cells and cells transfected with the lamin A Del50 mutation increase lamin concentration in the nuclear periphery in response to shear stress. However, the same study reports that the presence of 30% of transfected cells co-existing in a normal (non-expressing) cell population is sufficient to produce an abnormal response to stress in the normal cells. Interestingly, the peripheral lamin increase in these cells is less pronounced when compared to both normal and transfected cells, reflecting decreased lamin A/C remodeling. In line with these findings, the total lamin intensity, which reflects expression of lamins, increases more in response to prolonged shear stress in normal cells than in transfected and normal cells co-existing.

Morphological nuclear changes in response to shear stress were also significantly more pronounced in the control cells than in the co-existing condition. While normal cells become less circular and more elongated, changes in shape in transfected cells are much less pronounced; remarkably, the circularity of non-expressing cells practically does not change, but elongation does. These observations reinforce the premise that the presence of stiffer nuclei with impaired mechanoresponse can have an impact on how nearby normal cells respond to stress, attenuating their ability to adjust to the stimulus in an even more pronounced manner than cells with the lamin A Del50 mutation.

Considering the current knowledge on structure, physiology and mechanisms of mechanotransduction in a monolayer presented in this section, there are reasons to believe that both nuclear morphology and nuclear motion dynamics will be affected in the presence of cells with stiffer nuclei and impaired mechanoresponse, due to imbalance of forces.

2.2 Computational methods in biological analysis

Computational microscopy bioimage analysis has long been established as a tool for cell characterization and used in basic and clinical research. Intensity values and distribution, cell or nuclear morphology and migration can all be assessed using computational analysis in a high-throughput manner. As an alternative to manual analysis, it is less cumbersome, more objective and large volumes of image data can be processed efficiently, possibly minimizing erroneous conclusion stemming from outlier behaviour. These tools allow inference about cellular phenotype and behaviour, molecular landscape and complex physiological mechanisms, in spite of the many technical drawbacks which can still be pointed out.

The general workflow involved in the computational processing of microscopy bioimages is described in Figure 2.3. Upon the collection of biological data, computational processing will often involve 3 steps: collection of objects/ROIs, feature extraction and feature selection. The most common techniques are presented below.

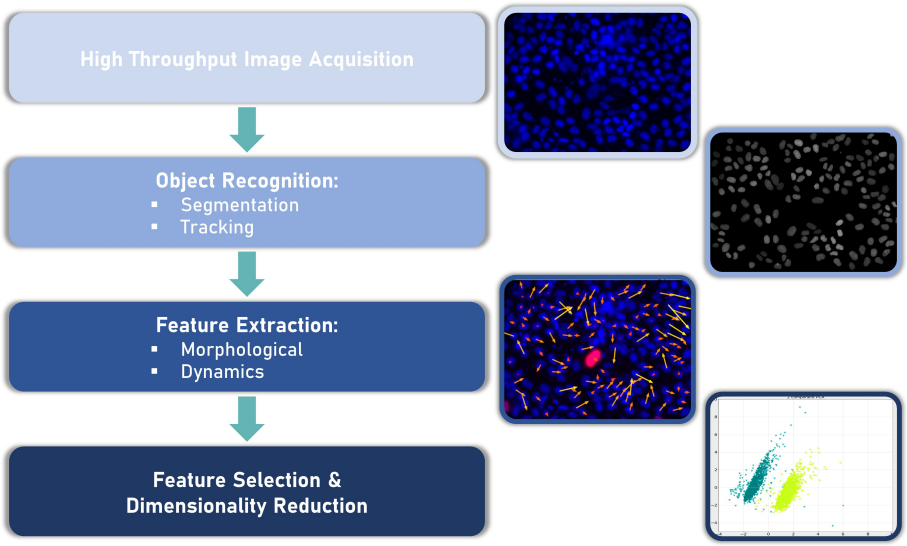

Figure 2.3: Workflow for the generation of cellular or nuclear phenotypic profiles, adapted from [33].

2.2.1 Nuclear segmentation and tracking

Once biological data is imaged, namely regarding monolayers of cells or tissues, segmentation and tracking of cells or nuclei is commonly the following step in the analysis. For segmentation, two main tasks are required - nuclear discrimination from the background and nuclear separation. Tracking involves associating segmentation masks along time. These are often bottleneck stages in image processing, where both biological and technical variability can hinder performance.

These tasks will usually either require high levels of human input or high levels of configuration and customization for each individual experiment. This is antagonist to the development of high-throughput methods of segmentation. Some of the most popular bioimage processing tools [34] which help with automation include Fiji [35], CellProfiller [36] and Icy [37].

Two main approaches are used for segmentation. The edge-based approach locates discontinuities in the image, assumed to correspond to the border of the ROI; the region-based approach, alternatively, achieves segmentation by assuming homogeneity of the ROI [2]. Methods commonly used for segmentation of fluorescent microscopy image data include filtering (gaussian blur for smoothing, variance for edge enhancement), which is often a preprocessing stage along with techniques for Signal-to-Noise Ratio (SNR) enhancement; global or local adaptive thresholding [38]; watershed [39]; or active contour [40] algorithms. While many tools are available, and even if image data collection is performed to the best of the available conditions, segmentation will usually involve manual adjustment of parameters, either according to the dataset or even within one dataset, due to heterogeneity of the samples or the occurrence of technical artifacts [41].

Cell tracking in turn requires identification of ROIs and maintaining of their identity throughout the image data sequence. Challenges to cell tracking, namely in fluorescent microscopy, relate to the low SNR, non-homogeneous transfection or staining, photobleaching or uneven background, among others [42]. Manual tracking is possible, but cumbersome and with low precision.

Tracking models can usually be placed into two categories: tracking by detection (where the first step consists on the detection of the ROIs in every time frame, and the second step involves an optimization strategy which determines correspondence of ROIs across time) [43] or tracking by model evolution (both tracking and segmentation are performed simultaneously, and the final result of one frame is used as the initial condition of the following frame) [44]. Many techniques are available, however, often integrated in the aforementioned bioimage analysis software [45].

Ideally, a segmentation and/or tracking model should be able to properly segment nuclei without the need for manual adjustment, regardless of the image type or experimental conditions - fully automated, generic and robust. Modern approaches to the segmentation and tracking problem often make use of machine learning strategies [46], or even deep learning [47]. While these models have been shown to perform better than other classical methods [48], annotation of datasets and training of the net is burdensome and technical variability in data collection continues to be a challenge due to overfitting.

2.2.2 Nuclear morphometry

The characterization of cell phenotype and dynamics can be used to describe cell mechanisms and processes (such as the cell cycle), to monitor cell development (cell differentiation and aging) or as a tool for diagnosis [1]. Nuclear shape varies according to cell type and stage of the cell cycle, but these organelles are generally ellipsoid or spheroidal [8]. However, shape can change in accordance to functionality of the cell, *e.g.* to potentiate transmigration [13]; these alterations may also be indicative of pathology. Namely in cancer, cells are usually identifiable by displaying abnormal morphology or stiffness [3, 28]. Nuclear morphometric analysis, then, emerges as a powerful resource due to the ability to relate the shape of the nucleus with several physiological or pathological mechanisms [49].

A quantitative, objective description of nuclear shape and trajectory can easily be achieved and unveil phenomena which cannot be detected by observation. Machine learning can also be applied for this type of analysis, namely for feature selection, dimensionality reduction or outlier detection [33]. More recently, 3D dynamic shape analysis [50] opens the path to a more detailed understanding on how cell shape varies according to physiology and function.

The present work makes use of a large array of computational feature extraction methods in order to capture the complexity of nuclear morphology and dynamics. While common methods are used, a technique to provide detail on the evolution of the nuclear boundary is also developed. A more detailed description and background are provided in Chapter 3.

3

Methodology

Contents

3.1 Preparation and acquisition of biological data

Data collection and processing can be divided into three main stages: preparation of biological data and imaging (each image contains a time series of one Field-of-View (FOV) of interest), preparation of digital data (preprocessing to obtain nuclear intensity masks and coordinates of nuclear centroids over time) and processing (with the aim of analysing nuclear morphology and dynamics, including collective cell migration). Methodology is described with detailed in the sections below.

3.1.1 Cell Culture and Transfection

Normal Rat Kidney Epithelial (NRK-52E) cells were cultured in DMEM media (Thermo Fisher) supplemented with 10% FBS and imaged +2 days after plating. For the mutant nuclear variant, cells were transfected with a plasmid for Del50-LMNA-TagRFP [20] +1 day after plating, using standard lipofection according to manufacturer protocols.

Two types of cell culture were prepared: one setting contained only normal NRK-52E cells; the second contained both normal, non-expressing NRK-52E cells and a small percentage of transfected, mutant NRK-52E cells, sparsely placed.

3.1.2 Imaging

Prior to imaging, cells were stained with 0.2μM Hoechst 33342 (1:5000 dilution) in DMEM media for 10 minutes. Subsequently, cells were washed with PBS and imaged in OptiKlear imaging media (VWR). Imaging was conducted on a Leica DMI 6000B with incubation at 37°C, using a 40X 1.25 NA objective, at 3 minute intervals over the course of 1 hour following a previously published protocol [20].

Each image collected represented a time-series composed of a a total of 21 frames. The dimensions of each frame are 696x520 px (2.1705 pixel/μm) in a total of 5 Z-slices.

A set of 10 images (each corresponding to one temporal sequence) was collected regarding the control monolayer (Control (C) or WT cells) and two sets (9 and 5 images, respectively) were collected in the monolayer with M cells and Non-expressing (NE) cells (M +NE condition), minding the placement of M cells in two ways: firstly, the M cell(s) in-frame should be as close to the center as possible; secondly, assuring that out-of-frame M cells were not close to the imaged area. This allows for a distance-dependent analysis of the behaviour of NE cells surrounding M cells. The images for the first condition images (C cells) display only the blue (Hoechst 33342) channel, whereas the second condition (M + NE) includes both blue and red (expression of Del50-LmnA-TagRFP) channels, which allow for the segmentation of nuclei and identification of lamin A Del50 expressing cells. The red channel is used only for the latter purpose and following sections refer to processing on a grayscale image corresponding to the Hoechst 33342 channel.

3.2 Data preprocessing

The biological data collected contains 3 groups of nuclei whose characterization is of interest. First, one would like to study the behaviour and features of nuclei in a control setting, *i.e.* normal cells in a monolayer. This group (C) will allow for the assessment of how the second condition under study, the presence of mutant cells within a monolayer of normal cells, affects nuclear behaviour and characteristics of the monolayer. Thus, the second condition yields two groups of interest: cells with stiffer nuclei (M) and normal cells surrounding the monolayer defects (NE). Preprocessing of the images, segmentation and tracking of the nuclei were performed using the same methods across all groups of interest, with maximal automation, in order to guarantee consistency in data collection and minimize erroneous conclusions stemming from human verification errors.

An overview of the process can be seen in Figure 3.1. This is the result of an empirical approach to image analysis, with a starting point defined by some of the most frequently used methods for segmentation and tracking but where the aim was to both automatise but standardise the processing methodology, *i.e.* finding a method which is able to segment nuclei in all the images collected, instead of changing the approach from one dataset to another, whilst requiring minimal manual input. While both software used (Fiji and Icy) provide plug-ins which can achieve segmentation and tracking, the combination of the two (Icy offers an interface with ImageJ - on which Fiji is based - so processing can take place all in the same application) was able to provide the best results.

3.2.1 Contrast Normalization

The first preprocessing steps towards achieving an accurate segmentation and tracking were performed using Fiji [35], an open-source Java-based ImageJ software commonly used for the analysis of biological images. Since a 2D analysis of a time series was the objective, a Z-projection of the images was required, in order to collapse this dimension. The method used for flattening the images was maximum intensity projection, where each pixel of the resulting image represents the maximum value of all the pixels in the same position, along the Z direction. While this assures that the nuclei are flattened in such a way that conserves their brightness in all their area, the maximum intensity projection will also conserve information from out-of-focus planes and the resulting image may appear ”blurry” as a result. In order to circumvent this fact, only planes where the majority of the nuclei were in focus were kept and used for projection. Because analysis of intensity distribution on the nuclei was not intended, but rather an analysis of shape and morphology, inconsistencies on the number of Z planes included in each image do not influence downstream analysis.

Following this step, image contrast normalization is applied. This method is based on the calculation of block statistics from summed-area tables, using integral filters [51]. The block radius used was 10

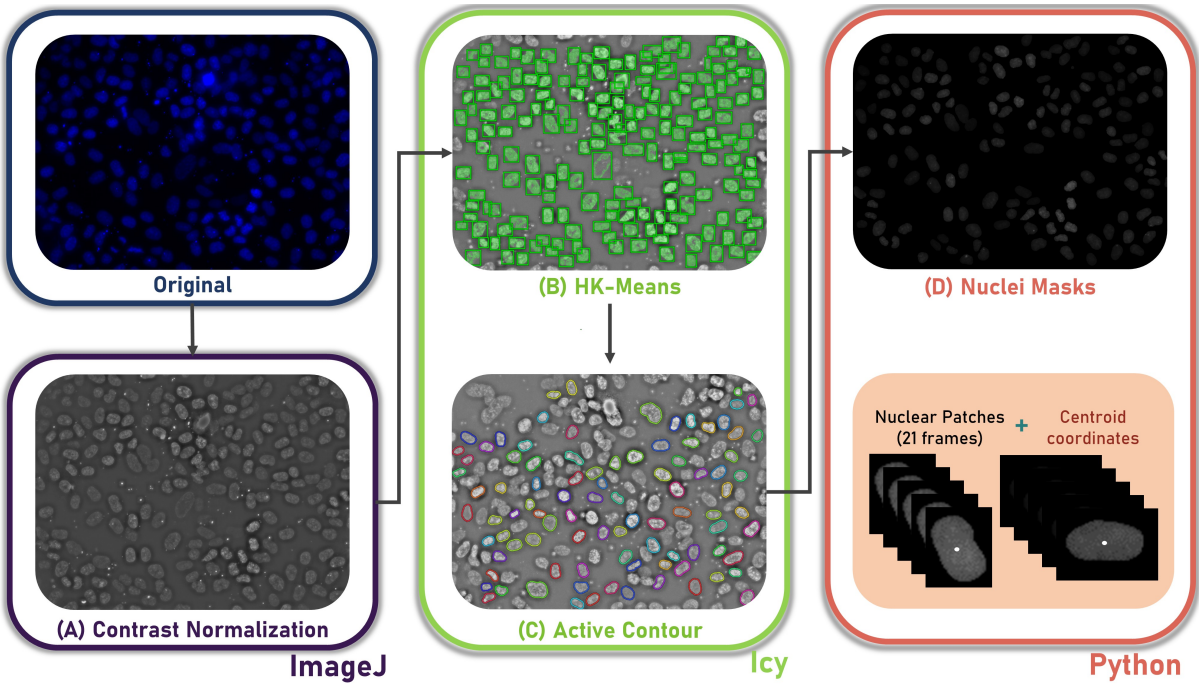

Figure 3.1: Overview of image processing methods used to obtain the intensity masks of each nucleus. A preprocessing step on *ImageJ* includes contrast normalization of the image stack (A), which is then input to *Icy*, where the remaining preprocessing takes place. Initial segmentation is achieved by the use of a Hierarchical K-means (HK-means) method (B), which serves as reference for the application of an Active Contour plug-in, accomplishing accurate segmentation and tracking of nuclei across the 21 frames (C). Finally, the region outside of the nuclei masks is zeroed and an image stack containing only the nuclei of interest is obtained, which is used for processing and feature extraction.

pixels in both x and y dimensions, and centering was applied. Integral images are at the basis of methods such as Speeded-Up Robust Features (SURF) [52], used for object recognition and tracking; in this particular case, it reduces the contrast between the nuclei and the background but the blurring caused by the projection of out-of-focus nuclei takes values of intensity which are smaller(darker) than those of the nuclei and the background (see Figure 3.1 A). While previously the blurring resulted a gradual decrease of intensity from the ROI - the nucleus - to the background, the normalized image contains ROIs where borders are now defined by abrupt decreases in the value of intensity. One can theorize that this fact will contribute to the success of the application of the Active Contour plug-in, further detailed below.

3.2.2 Hierachical K-Means Segmentation

The normalized 2D time series, for this and following steps, are processed using Icy [37], also an open-source Java-based platform which specializes in biological image analysis and offers a number of plug-ins.

Figure 3.1 B illustrates the result of using HK-means [53] to obtain an *initial* set of segmentation

masks for each of the images. This is a region-based segmentation method which takes the histogram of intensities of an image and produces a predefined number of clusters which represent different intensity classes. Each of these clusters corresponds to a threshold for which a binary image can be produced. A minimum and maximum dimensions of the objects of interest can be set by the user. A bottom-up approach is adopted as each threshold is applied to the image and only objects within the dimension of interest are kept.

An additional parameter was used to define the initial masks: minimum object intensity, which excluded segmentation areas corresponding to the background. The use of this method, although more practical and with better performance than the use of manual thresholding, comes with a few drawbacks, namely difficulty in separately segmenting nuclei that are very close/overlap and difficulty in properly segmenting a very heterogeneous nucleus - since there are many different intensity levels, one nucleus can be defined by several segmentation masks. As a consequence, following the application of HK-means there is the need to manually adjust the initial masks, by removing those who do not refer to ROIs and separating those who refer to nuclei that are close but do not overlap.

On this note, segmentation and tracking are also hindered by characteristics of image collection and biological behaviour. The main factors contributing to invalidate segmentation include: non-uniform distribution of average intensities of nuclei, *i.e.* in the same image, different nuclei will have the different intensity levels, which sets back the use of a straightforward thresholding method to segment all nuclei; the occurrence of overlapping nuclei along the time series; and the existence of ”floating” stain speckles, of high intensity and whose migration is unlike that of the nuclei, which can also partially overlap with one or several nuclei along the time series and hamper segmentation, by being interpreted as a part of the nuclear shape.

3.2.3 Active Contour Model

The final segmentation masks (which correspond, in fact, to outline polygons of the ROIs - see Figure 3.1 C) are obtained using the Active Contours (AC) plug-in [44], on Icy. This model, also called *snakes*, was initially proposed by Kass et al. [40] and has shown great results as a segmentation method [2]. It uses discrete explicit representations of the curves (contours in 2D, surfaces in 3D) in an energy-minimizing framework. Energy, here, is defined by internal terms - regarding deformation/evolution of the curve, namely smoothness and continuity - and external terms, referring to data from the image (intensity, gradient). Segmentation is achieved via the minimization of this energy function, which will converge to a local minimum if using the Euler-Lagrange steepest gradient descent.

The method is initialized with the HK-means masks, in the first frame of each image, from which the contours are drawn before they begin progressively deforming into the edges of the nuclei. The AC method is relatively fast, as it takes the contours of a previous frame as reference for tracking and

segmenting in the following frame.

Due to prior image preprocessing, the default user-defined parameters selected to run the AC method are used. Edge and region weights represent the expected intensity difference at the border of the ROI and the homogeneity of intensities within the ROI, when compared with the background. The values 0 and 1 were used, respectively, indicating minimum intensity difference and maximum intensity homogeneity - which could potentiate a conservative approach to contour evolution. The contour smoothness ($[0, 1]$) was set to 0.05 - although nuclear shape is mostly smooth, it is useful to run the algorithm with little assumptions on nuclear shape, in order to avoid biasing the results. Finally, evolution parameters define contour sampling precision (2 px), evolution time step (0.1) and convergence criterion (0.001 - a higher value leads to a faster run time but may cause loss in performance).

While this method performs quite well and runs relatively fast, several nuclei were poorly segmented, mainly due to the previously mentioned overlap of nuclei and of debris. Therefore, manual correction was necessary for this step as well, excluding all of the nuclei in which segmentation in *any* of the 21 frames was not satisfactory. While some cases of mitosis can be successfully segmented and tracked using the proposed pipeline, for the purposes of the downstream analysis this data was not necessary and thus all the nuclei in mitosis during the time series were excluded as well.

Furthermore, for the images with the M+NE nuclei, NE nuclei with a distance to the image border inferior to 50 μm were excluded, thus conserving only nuclei more close to the center of the image, in order to not jeopardize a distance-dependent analysis by the presence of closer but out-of-frame M cells.

From the remaining contour curves, two types of data were extracted: the nuclear intensity masks (Figure 3.1 D), where to each nucleus correspond 21 binary masks (one per time frame), which are zero everywhere outside of the ROI and whose dimensions are those of the bounding box of the ROI for each frame; and the centroid of each bounding box along the time series, in order to account for tracking. Because the contour (obtained with the AC plug-in) is defined by a number of points which varies in proportion to perimeter, and because these points don't have to overlap with pixels but can be placed anywhere in the image, both the bounding boxes and the centroids have decimal precision.

3.3 Feature Extraction

The intensity matrices and tracking information were analysed and processed using Python. Because intensity distribution was not the main focus of the analysis, but rather morphology and migration, there was no need to normalize nuclear intensity across datasets. As was mentioned, three groups of interest were analysed: C (control, all-normal monolayer) nuclei, M nuclei and NE nuclei.

In order to characterize the monolayer from both a static and dynamic perspectives, three main sets

of features were extracted (see Figure 3.2): migration features, static shape/morphological features and dynamic shape/morphological features (or morphological variation features). Below is a brief description of the calculation and interpretation of each one.

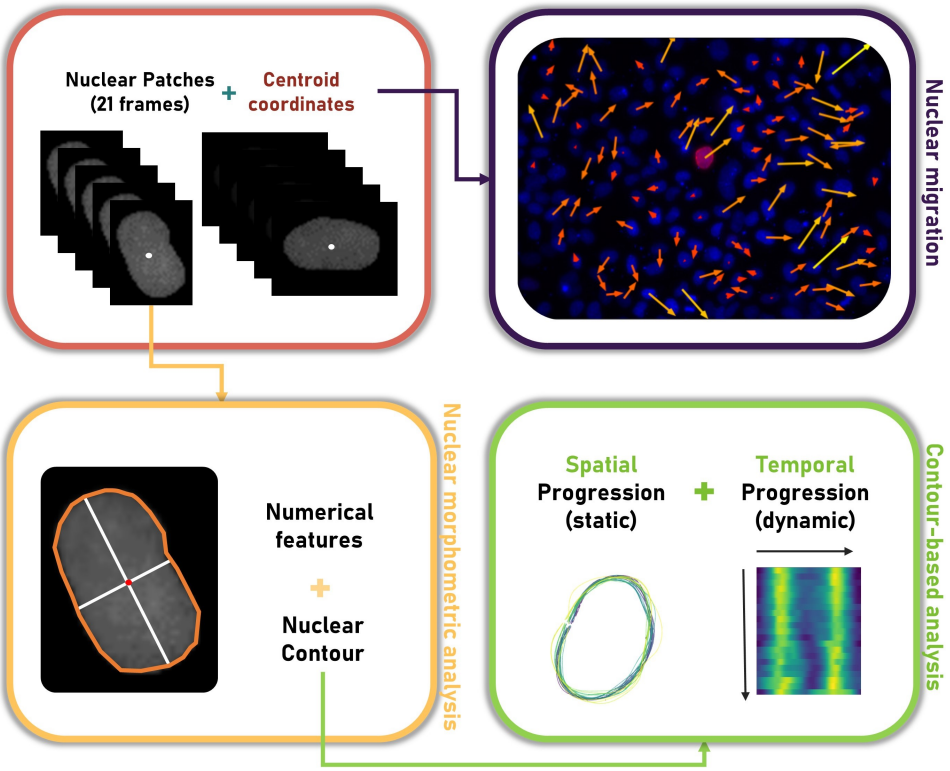

Figure 3.2: Three sets of features are extracted from the nuclear masks and centroid coordinates obtained from the preprocessing of data. Nuclear motion is characterized from the evolution of centroid positions (blue box) and the intensity masks provide both the basis for the nuclear morphometric analysis (orange box) and for the nuclear boundary extraction, which allows for the analysis of spatial and temporal evolution of the nuclear membrane (green box).

3.3.1 Monolayer Dynamics Features

In order to understand how the presence of mutant cells is influencing monolayer dynamics, some features can be calculated regarding cell motion speed and direction. Formulas are displayed on Table 3.1.

Orientation of the nuclei is defined by the angle between the horizontal axis and the major axis of the ellipse that has the same second moments as the region. It ranges from $-\pi/2$ to $\pi/2$, counter-clockwise. Absolute orientation variation is calculated by the absolute difference in orientation in subsequent frames, divided by the interval in minutes between frames. It characterizes rotation changes in a nucleus, giving a sense of ”velocity of rotation”.

Direction is similar to orientation but it describes orientation of motion rather than rotation of the nucleus. It is measured as the angle between the horizontal axis and the vector whose start and end

Table 3.1: Nuclear motion features calculated for each nucleus.

Feature	Formula	
Absolute Orientation Variation (rad/min)	$\Delta_\phi = \frac{1}{\Delta t}\frac{\sum_n^{N-1}\lvert\phi_{n+1}-\phi_n\rvert}{(N-1)}$	N - total number of frames Δt - time (in min) between frames ϕ_n - orientation on frame n (rad).
Direction Variation (rad/min)	$\Delta_\psi = \frac{1}{\Delta t}\frac{\sum_n^{N-2}(\psi_{n+1}-\psi_n)}{(N-2)}$	ψ_n – direction of trajectory, defined as the angle between position on frame n and position on frame $n+1$ (rad).
Mean Step Displacement (μm/min)	$v = \frac{1}{\Delta t}\frac{\sum_n^{N-1}\sqrt{(x_{n+1}-x_n)^2+\ (y_{n+1}-y_n)^2}}{(N-1)}$	x_n, y_n - coordinates of the nucleus centroid on frame n.
Total Distance (μm)	$D_T = \sum_n^{N-1}\sqrt{(x_{n+1}-x_n)^2+(y_{n+1}-y_n)^2}$	
Net Displacement (μm)	$D_N = \sqrt{(x_N-x_1)^2+(y_N-y_1)^2}$	
Migration Efficiency	$\eta_D = \frac{D_N}{D_T}$	

points are the centroids of the nucleus in subsequent frames. So, while orientation refers to nuclear rotation, direction reflects nuclear translation. Accordingly, direction variation is the absolute difference between trajectory direction in subsequent frames, divided by the interval in minutes between frames.

Mean step displacement characterizes translation velocity. It is given by the euclidean distance between the position of the centroid of the nucleus in subsequent frames, divided by the interval in minutes between frames. Total distance takes into account only translation distance, and it is the sum of all the nuclear (euclidean) displacements in a time series. Conversely, net displacement is simply the euclidean distance between the initial and final coordinates of each nucleus, not reflecting intermediate nuclear motion. Finally, migration efficiency measures the ratio between net motion and total motion: if the nucleus moves in a straight line, efficiency is 1. If, however, the trajectory includes changes in direction, causing total distance to increase, migration efficiency will decrease as a consequence.

3.3.2 Morphometric Features

Table 3.2 contains the formulas used to analyse and compare nuclear morphology, based on the nuclei intensity patches. These features were calculated for all nuclei, across all time frames. Figure 3.3

illustrates in a scheme the main geometrical concepts involved in the calculation of these features.

Table 3.2: Morphological features calculated for each nucleus. Illustration of variables in Figure 3.3.

Feature	Formula	
Area	$A = \sum_i b_i$	b_i - value of pixel i in nucleus binary mask ($\{0, 1\}$).
Perimeter	$P = \sum_i c_i$	c_i - value of pixel i in nucleus contour binary mask, using a 4-connectivity($\{0, 1\}$).
Aspect Ratio	$AR = \frac{mAL}{MAL}$	mAL – Minor Axis Length of the ellipse that has the same normalized second central moments as the region. MAL – Major Axis Length of the ellipse that has the same normalized second central moments as the region.
Eccentricity	$E = \frac{FD}{MAL}$	FD – Focal Distance of the ellipse that has the same second-moments as the region.
Circularity	$C = \frac{4 \times \pi \times A}{P^2}$	
Roundness	$R = \frac{4 \times A}{\pi \times MAL^2}$	
Smoothness	$S_P = \frac{P_C}{P}$	P_c – Perimeter of convex hull.
Solidity	$S_A = \frac{A}{A_C}$	A_c – Area of convex hull.

Aspect ratio provides a sense of how elongated the nucleus is. Higher aspect ratios point to less elongated nuclei. Eccentricity, similarly to aspect ratio, refers to the general shape of the nucleus, which is approximated to an ellipse. In this case, FD is 0 if the nucleus is circular (zero eccentricity) and its value increases as the shape becomes more elongated. As such, eccentricity and aspect ratio are nearly inverse: a more elongated nucleus will have higher eccentricity but lower aspect ratio.

Circularity is a measure of area-to-perimeter ratio. For a perfect circle, circularity is 1. Circularity can decrease as the nucleus becomes more elongated; however, as perimeter increases or area decreases (due to a more irregular boundary or shape), circularity will decrease as well, reflecting concavity of the nucleus. The feature roundness is similar to circularity but, unlike the latter, where the area of the nucleus is compared with its perimeter, the calculation of roundness compares the area of the nucleus with its “convex perimeter” – where the nucleus is assumed to be circular and taking its major axis length as a measure for the diameter. This makes roundness insensitive to perimeter irregularities and thus a more direct measure of structural shape.

Finally, smoothness and solidity make use of the calculation of the convex hull of the region and reflect ratios between its perimeter and area and the perimeter and area of the original ROI. Smoothness is also known as “convexity”. A completely convex shape will take the value 1, and smoothness

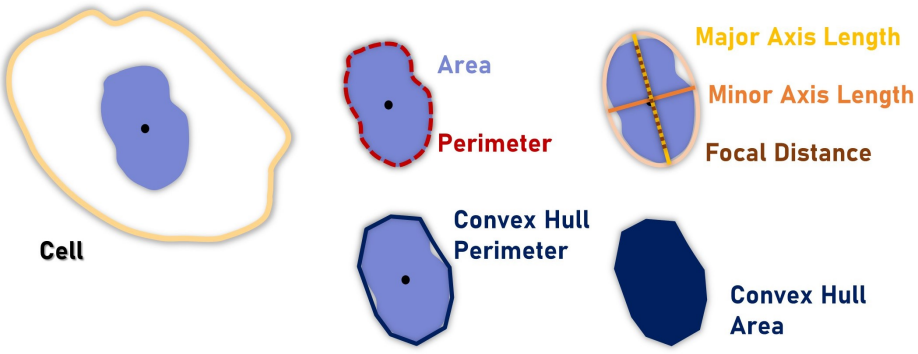

Figure 3.3: Main geometrical definitions for the calculation of morphometric features. The nucleus is represented in light blue, with the centroid as a black dot. Area and perimeter are directly measured from the binary mask of the nucleus. The convex hull corresponds to the smallest convex polygon that encloses the region of interest. From the ellipse that has the same normalized second central moments as the region (pink, upper right), major and minor axis length can be determined, as well as Focal Distance (FD) (distance between focal points, such that for any point p of the ellipse the sum of the distances to the focal points is a constant. In a circle, FD is zero because the two focal points overlap with the centre).

decreases as the nucleus becomes more concave or its boundary more irregular. Similarly, solidity measures ”density” of a nucleus. While a solid object (such as a circle) will have solidity equal to 1, more irregular nuclei will have lower solidity values. The two features are related but reflect different shapes. For example, a nucleus whose boundary is very irregular but these irregularities have very small amplitude (*i.e.* numerous but small blebs) will have solidity close to 1 (the convex hull and original shape have similar values for area) but a lower value of smoothness, as the perimeter of the original shape is higher than that of the convex hull.

3.3.3 Contour-based Features

Membrane fluctuations have been shown to reflect mechanical properties of cellular components and many methods have been developed with such purpose [54]. Here, a contour analysis is performed from fluorescence microscopy data, with the objective of characterizing the nuclear boundary in more detail and to provide a more intricate numerical description of morphology dynamics.

First, the boundary for each nucleus was transformed in polar coordinates (ρ, θ), according to distance to the nuclear centroid, for each time frame. This corrects contours for translation (Figure 3.4 I a)). Then, the contours are corrected for rotation, *i.e.* all the nuclei are rotated until their major axis corresponds to the vertical axis ($\theta = \pm\pi/2 = \pm 180°$) (Figure 3.4 I b).

In order to numerically compare the boundaries for each nucleus across time, and in order to compare different nuclei within the same group and across groups, a cubic spline interpolation (more details on Figure A.1) was applied to the polar coordinates, and every boundary became defined by a set of

100 points, corresponding to the same values of θ (Figure 3.4 II)).

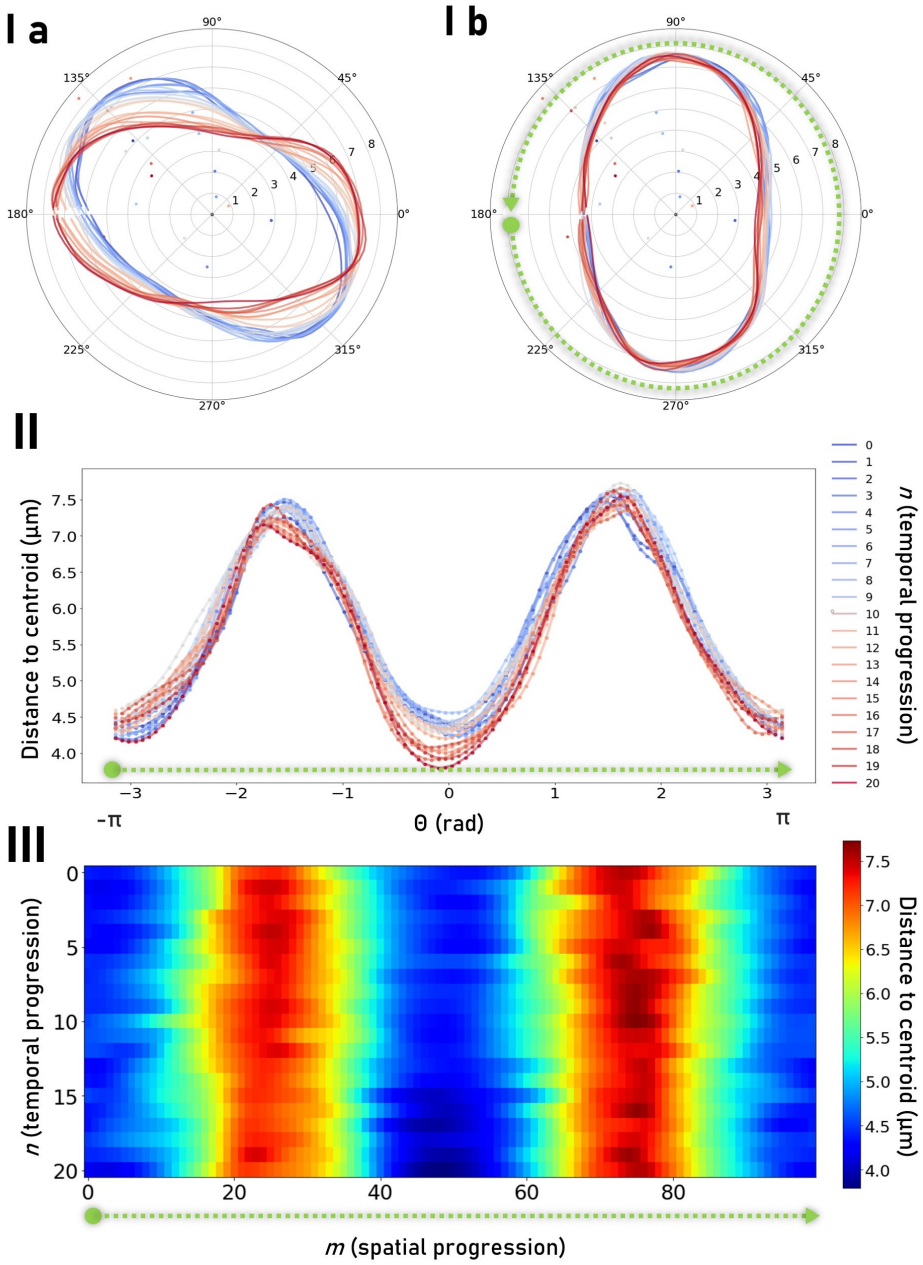

Figure 3.4: Data processing for numerical contour feature extraction. I) Polar representation of nuclear boundaries. Each curve corresponds to the boundary in one frame, with the centroid in $(0, 0)$. Position of the original centroid of each frame in relation to the average centroid location of the nucleus can be seen as data points of the corresponding color; a) represents translation correction and b) corresponds to rotation correction. Angles in degrees, distance to centroid is in μm. II) Cubic spline interpolation results, for one nucleus. Curves represent initial contours and markers represent new contours, after interpolation, defined by 100 datapoints. III) Matrix representation of temporal and spatial progression of the nuclear boundary, coloured according to distance to centroid. Green arrows help interpretation of matrix-like representation of the contour profile.

Several features can now be calculated, regarding spatial and temporal progression of the nuclear boundary. One can imagine this progression represented in a N×M matrix, where N represents the total number of frames in the time series (21) and M represents the total number of points in the boundary (100), referring to the θ variable (Figure 3.4 III)). Contour magnitude is represented as values in this matrix. Analysing row-wise gives spatial progression or contour "static" regularity, *i.e.* how distance to the centroid varies for different values of θ. Column-wise analysis will provide information on temporal progression or contour "dynamic" regularity, *i.e.* for the same θ, how distance to the centroid evolves over time. A completely homogeneous matrix, for instance, would represent a perfectly circular nucleus which is absolutely rigid, meaning its boundary does not change over time. Table 3.3 contains the formulas used to quantify boundary aspect and fluctuations, with analogous sets of features for spatial and temporal progression. These features are further illustrated in Figure 3.5.

Table 3.3: Contour-based features calculated for each nucleus. $r_{m,n}$ is the contour value, or distance to the centroid (ρ), for boundary position m at time n (in μm).

Feature	Formula	
Contour Range	$R_s = \frac{1}{N}\sum_n^N \frac{r_{max,n} - r_{min,n}}{r_{max,n}}$	$r_{max,n}$,$r_{min,n}$ - maximum (resp. minimum) radius across boundary for time frame n.
Contour Amplitude	$\Delta_s = \frac{1}{N \times (M-1)}\sum_n^N \sum_m^{M-1} \lvert\frac{r_{m+1,n} - r_{m,n}}{r_{m,n}}\rvert$	M – total number of points in spatial boundary (100).
Contour Abruptness	$S_a = \frac{1}{N}\sum_n^N \max \lvert\frac{r_{m+1,n} - r_{m,n}}{r_{m,n}}\rvert$	$m \in [1, M-1]$
Curvature	$\partial s(n,m) = \frac{r_{m+1,n} - r_{m,n}}{r_{m,n}}$	$m \in [1, M-1]$ $n \in [1, N]$
Contour Concavity	$C_\partial = \frac{1}{N}\sum_n^N \sum_m^{M-1} [\partial s(n,m) < 0]$	
Temporal Contour Range	$R_t = \frac{1}{M}\sum_m^M \frac{r_{m,max} - r_{m,min}}{r_{m,max}}$	$r_{m,max}$,$r_{m,min}$ - maximum (resp. minimum) radius in each boundary point m, across time.
Temporal Contour Amplitude	$\Delta_t = \frac{1}{M \times (N-1)}\sum_m^M \sum_n^{N-1} \lvert\frac{r_{m,n+1} - r_{m,n}}{r_{m,n}}\rvert$	
Temporal Contour Abruptness	$T_a = \frac{1}{M}\sum_m^M \max \lvert\frac{r_{m,n+1} - r_{m,n}}{r_{m,n}}\rvert$	$n \in [1, N-1]$

Contour range is the difference between maximum radius (ρ, the distance from the centroid to the nucleus boundary) and minimum radius, divided by maximum radius for normalization purposes. A perfect circle would have zero amplitude, while a very concave or elongated nucleus will have large

contour amplitude. This is, then, a measure of spatial progression and could be related to concavity of the nucleus.

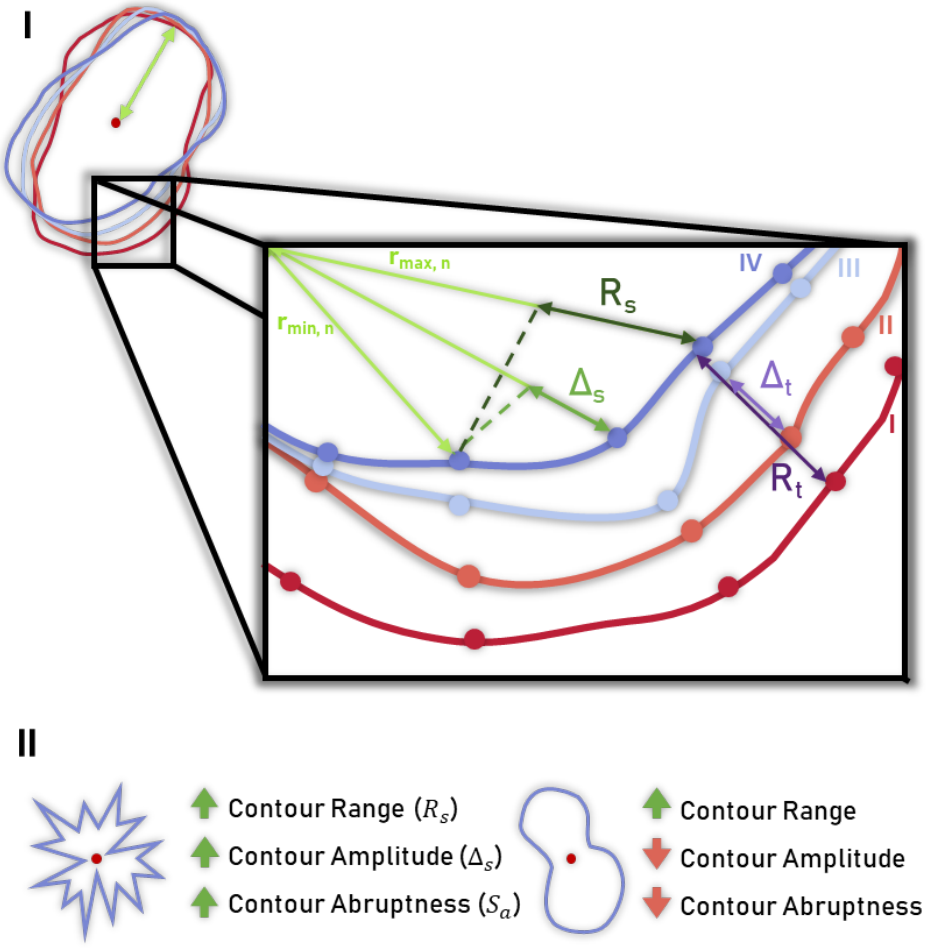

Figure 3.5: I) Simplified representation of contour-based features from Table 3.3, for a nucleus with 4 time frames (I-IV). Centroid in dark red. Δ_s is the difference in radius between subsequent points of the nuclear boundary. The maximum difference for one time frame is S_a. R_s is the difference between maximum and minimum radii. Temporal analysis concerns one boundary point across time. Δ_t is the difference between subsequent frames. The maximum Δ_s corresponds to S_s. R_t is analogous to R_s but across time. Note that features used in the analysis are averages across time or space and are normalized, unlike what is shown here. II) Illustration of nuclear aspect for different values of spatial features.

Contour amplitude, in turn, is the difference between subsequent radius ($r_{m,n}$, characterized by a position m at time point n), divided by $r_{m,n}$ (again, for normalization purposes). This value is averaged across the boundary and across time, to provide a sense of mean spatial progression of the nuclear boundary. Very abrupt contours will have high values of contour amplitude.

Contour abruptness relates to contour amplitude. It is defined by the maximum contour amplitude between subsequent points of the nucleus boundary. A nucleus with abrupt irregularities will have a higher value of abruptness, whereas a smooth nucleus will display lower abruptness. Note that a

very concave nucleus (high contour range) can have low contour abruptness, if the range of variation observed stems from a smooth boundary spatial progression (see Figure 3.5 II).

Curvature is a proxy for boundary derivative, as the relative changes in boundary radius are calculated. A nuclear boundary can be represented in a N$\times$M matrix, and its curvature will be fully characterized in a N$\times$(M-1) matrix. This will provide a sense of contour regularity. Following this definition, concavity is the time-average of the number of negative deflections in the boundary, *i.e.* the total number of negative values in the curvature for a given frame n.

Temporal contour range, here, serves as a measure of temporal progression. It will give a sense of "boundary softness" or "flexibility", *i.e.* how much the nucleus can change over time. It is equivalent to the feature R_s, but considers the general evolution of the nuclear boundary time-wise rather than space-wise.

Temporal contour amplitude and temporal contour abruptness are analogous to contour amplitude and contour abruptness, but for temporal rather than spatial progression. While temporal contour range defined *how much* nuclei are changing, amplitude defines *how* they are changing. Nuclei with a more constricted boundary will have smaller amplitudes of variation. Temporal contour abruptness contemplates both nuclear stiffness and regularity. If amplitude is low and abruptness is high, then the nuclear boundary mostly oscillates smoothly over time but maintains flexibility. If both values are low, then the ability of the nuclear envelope to adjust its shape may be impaired, which could be indicative of higher nuclear stiffness.

At this point, an additional, automatic step of segmentation verification can take place. Considering the *temporal* amplitude of each boundary of each nucleus, one can relate abnormally high values of amplitude to incorrect segmentation rather than nuclear behaviour, as these boundary fluctuations would be outside of physiological ranges expected in either of the conditions analysed. To the best of our knowledge, the physiological range values of nuclear boundary fluctuations have not been published, so an empirical approach was adopted.

Calculating the maximum value of temporal amplitude for each nucleus, the obtained distribution is heavily skewed to the right (as most nuclei will have small amplitudes of fluctuations). As such, an upper limit for outlier detection (UL) was defined as can be seen below (Equation (3.1)):

$$UL = Q3 + 1.5e^{3MC}IQR \tag{3.1}$$

where MC corresponds to the medcouple, often used to measure skewness, $Q3$ is the third quartile and IQR is the interquartile range [55].

Abnormally segmented nuclei were detected if their temporal variation across the boundary crossed the UL value in more than 5% of the boundary extension (an example can be seen on Figure 3.6). These nuclei were excluded from the analysis, providing a method of segmentation verification which is

automatic.

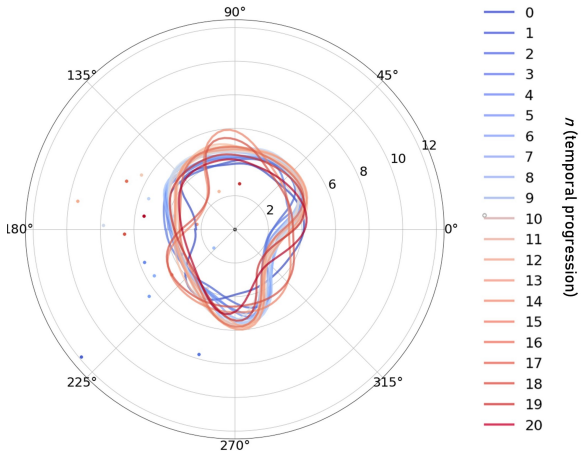

Figure 3.6: Example of nucleus excluded by automatic criteria post-feature extraction. Angles in degrees, distance to centroid is in μm. Nuclear shape evolution can be seen as curves in different colours.

3.4 Statistical Analysis

Confidence intervals for motion and morphological features are calculated as in Equation (3.2):

$$CI = \overline{X} \pm Z\frac{\sigma}{\sqrt{n}} \tag{3.2}$$

where n is the number of observations, $\overline{X}$ is the mean, σ is the standard deviation and Z is the Z-score value for the confidence level pretended [56]. A 95% Confidence Interval (CI) was used ($Z = 1.96$). If not represented in the figures, such intervals can be consulted in the tables on Appendix A.

All groups under study had $n > 30$ except for the mutant cells ($n = 20$, although for the static morphological analysis - Section 3.3.2 - all 21 frames of all nuclei were considered independent samples, thus for M nuclei $n = 420$). As such, under the Central Limit Theorem, normal distribution of values was assumed and statistical significance was assessed using a two-tailed unpaired t-test, without assumption of equal variance. P-values are represented using the standard scale ($ns - p > 0.05, *p \leq 0.05, **p \leq 0.01, ***p \leq 0.001, **** p \leq 0.0001$).

4

Results and Discussion

Contents

The following sections present the main findings of the present work. Detailed averages and significance testing can be found in Appendix A. These results reflect dependent phenomena (*e.g.* efficient cell movement requires nuclear motion and change in shape [23]) and, while causality is difficult to assess, the discussion will contemplate an overview of the phenotypic differences and how they could be correlated.

4.1 Data collection

Segmentation and tracking rendered a total of 2240 nuclei, after manual exclusion of nuclei with faulty segmentation and automatic exclusion of contour outliers. Population distribution per group can be seen on Table 4.1.

Table 4.1: Population of nuclei collected for each group, after exclusion of incorrect segmentation and tracking and automatic contour outlier detection.

Group	Population		Population (%)
C	918		40.98
M	20		0.89
NE	1302		58.13
	NE40	142	6.34
	NE80	368	16.43
	NE120	384	17.14
	NE160	288	12.86
	NE160+	120	5.36

In each image, an average of 57.27% and 63.11% of NE and C nuclei, respectively, were properly segmented and tracked. This is a rough estimate from the ratio between properly segmented nuclei across all 21 frames over the number of nuclei in the first frame of each image. Due to the high variability shown in performance by different segmentation and tracking methods, which depend on the proper selection of parameters and often cannot be generalized to any image type, it is difficult to compare the performance of the chosen method for segmentation and tracking with other state-of-the-art methods available. Such task would require burdensome testing of different approaches on the dataset used for analysis, and adjustment of parameters to maximize the performance of each approach. Given than segmentation and tracking were not the focus of the current work, but rather the analysis of morphological and dynamic features of a statistically significant population of cells, such testing was not carried out. Manual segmentation of nuclei could also have been performed and compared with the masks obtained

from the methodology used for the present work, in order to objectively measure segmentation accuracy, but the same justification applies.

Proper segmentation requires nuclei to stay in-frame and to not overlap with other nuclei or with stain speckles. Frequent instances of small high-density nuclear clusters, as well as nuclear overlap (partially caused by the projection of the data into a 2D image), lead to a lower percentage of success. Note that, because morphology was a fundamental element of the analysis, algorithms used for discrimination of nuclei in a cluster (such as the watershed algorithm) could underperform or bias the results regarding shape deformation. As such, the option of not including nuclei which overlap was adopted.

Contour-based automatic exclusion was applied conservatively, in order to avoid excluding nuclei in which abrupt boundary shape changes were physiological and thus only 21 C nuclei and 24 NE nuclei were excluded using this process, with all the M nuclei conserved.

For the distance-dependent analysis, each NE nucleus was characterized by the minimum euclidean distance between its centroid and the centroid of an M nucleus in-frame (see Figure 4.1). A 40 μm radius difference was used to separate the group, as this guaranteed a minimum of 50 NE nuclei per distance-group per preparation (two M+NE monolayer preparations were analysed), except for the NE160+ group in the second preparation, which rendered only 14 nuclei. Group are named according to cell type + maximum nuclear distance, *i.e.* NE40 represents NE nuclei which are less than 40 μm apart from an M nucleus, NE80 contains nuclei which are between 40-80 μm and NE160+ includes all nuclei whose distance to an M nucleus is superior to 160 μm.

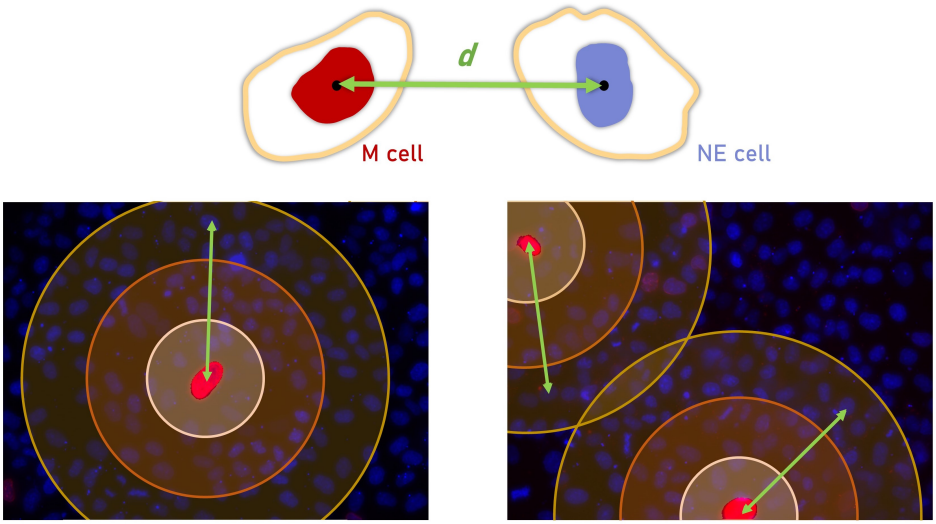

Figure 4.1: Illustration of group division in distance-dependent analysis. Top: schematic representation of how distance (d) between an M nucleus (red) and an NE nucleus (blue) is calculated. Bottom: nuclei within each coloured ring are part of a group characterized by a distance to an M nuclei between l_{min} and l_{max} of that ring. Where rings overlap, nuclei are attributed to group that is closer to an M nucleus. Rings are not to scale.

4.2 Monolayer dynamics

Collective cell motion was initially analysed and interesting differences were found between both monolayers, which are illustrated on Figure 4.2. Net displacement and total distance were normalized to the maximum value of the respective feature, in order to facilitate representation of the calculated features.

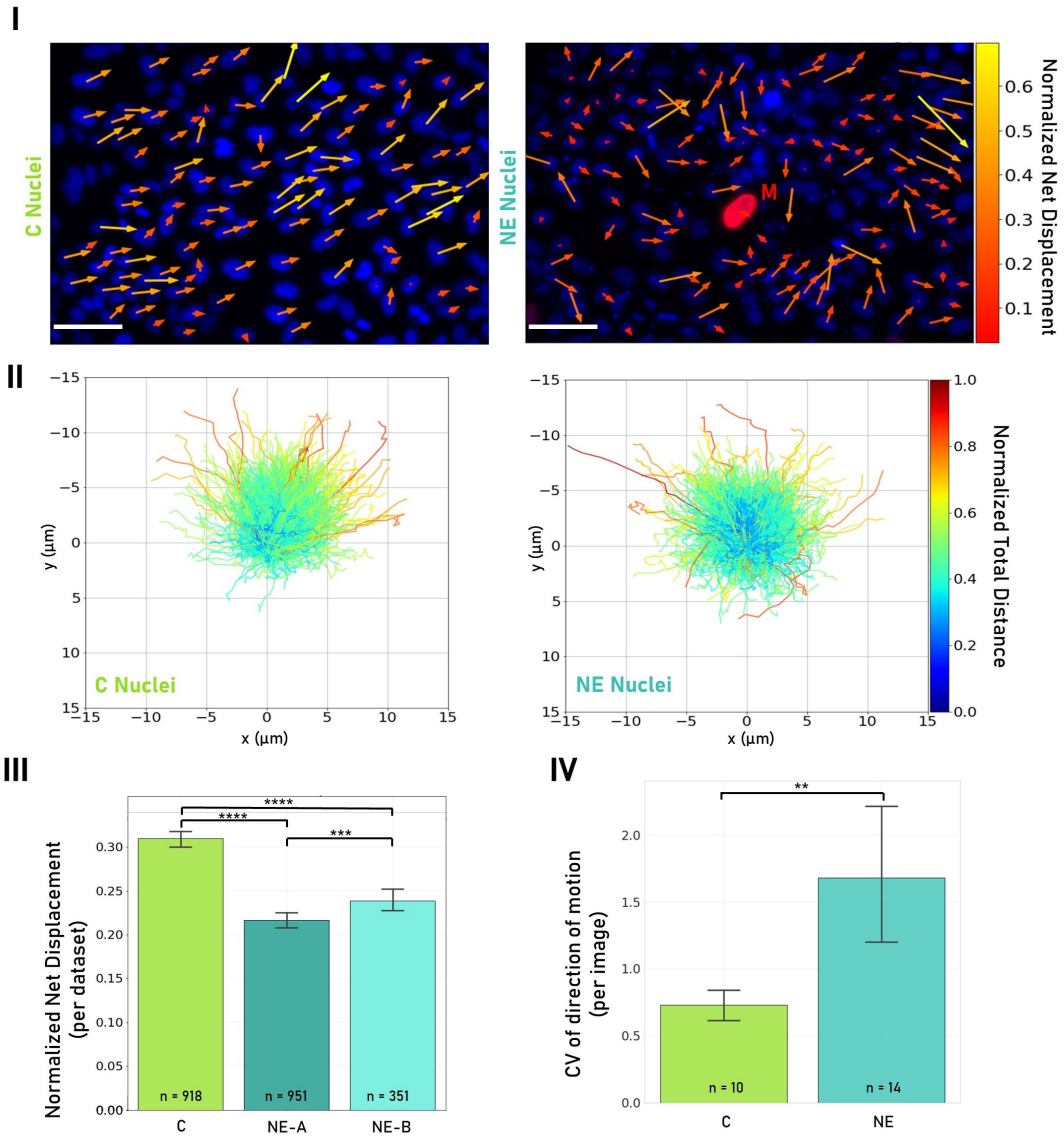

Figure 4.2: Monolayer dynamics are affected by the presence of M cells. I) On the left, a monolayer of normal cells (C), and on the right, a monolayer with normal cells (NE,blue) and one lamin A Del50 cell (M, red). Arrows are coloured and have a magnitude in proportion to normalized net displacement. Direction of arrows is determined by direction of net displacement vector. Bars represent 50μm. II) Migration "clouds", where the trajectory of each nucleus is represented and is coloured according to total distance. x and y coordinates are in μm. III) Net displacement is lower for both preparations of the M+NE monolayer, when compared to the control monolayer. IV) Direction of migration is less homogeneous in the M+NE nuclei than the C monolayer. Unpaired two-tailed t-test: $**p \leq 0.01, ***p \leq 0.001, ****p \leq 0.0001$.

Nuclear motion appears to be less coordinated in the M + NE monolayer. As a consequence, direction of movement is less homogeneous and net displacement decreases (Figure 4.2 I)). Figure 4.2 II) further supports these findings, by analysing both the shape of the ”migration cloud” - which represents direction of trajectories from its initial point, set at coordinates $(0, 0)$ - and its colour - which represents magnitude of total displacement. The NE nuclei cloud is more circular and nuclei with smaller values of total distance of migration are more prominent than in the C nuclei cloud. Interestingly, some NE nuclei have very long trajectories, indicating that both direction and magnitude of nuclear motion are more heterogeneous in the M+NE monolayer. Figure 4.2 III) reinforces the findings that the decreased net displacement is a consequence of the presence of M cells rather than a consequence of biological or experimental variability, as this phenomenon can be observed in both M+NE monolayer preparations (labelled A and B).

The Coefficient of Variation (CV) is defined as the ratio between the standard deviation and the mean value of a feature. It represents how ”spread” the values for that feature are - a smaller CV corresponds to a more homogeneous population. Figure 4.2 IV) shows the average CV for net direction of motion within one image. The direction of motion (angle between initial and final positions of each nucleus) of NE nuclei is less defined (the motion in that monolayer of cells is less coordinated), whereas the monolayer with only normal cells has nuclei which move in unison.

A distance-dependent analysis provides further insight into the dynamics of the monolayer and mechanical force transmission, as well as energy release (Figure 4.3). First, the findings already mentioned for the all-normal monolayer are confirmed. C nuclei move faster, rotate less than NE nuclei and change direction significantly less. As a consequence, migration efficiency is the highest amongst all groups analysed. By contrast, M cells have severely impaired nuclear movement. Their nuclei move slower than C nuclei, rotate significantly less and change direction more. Efficiency appears to be higher than NE cells, but it does not mean these cells are moving more but rather that the ratio between net displacement and total distance is superior to that of NE nuclei, implying that, while impaired, nuclear motion is still somewhat efficiently performed. NE nuclei, however, present a very curious behaviour. On average, these nuclei move faster than M nuclei but slower than C nuclei. They rotate and change direction more than both M and C nuclei, which in its turn leads to lower values of migration efficiency. However, the distance-dependent analysis reveals that this behaviour is not monotonously evolving in proportion to distance to an M nucleus, but rather there seems to be a compensatory and counter-compensatory behaviour which tends to balance abnormal motion introduced by the mechanically defective M cells. This can be observed both for the motion velocity (mean step displacement), direction variation and absolute orientation variation, although less pronounced in the latter. The closest nuclei to an M cell (NE40) move faster, rotate more and change direction more than the following group (NE80), which moves slower, rotates less and changes direction less than the next group (NE120).

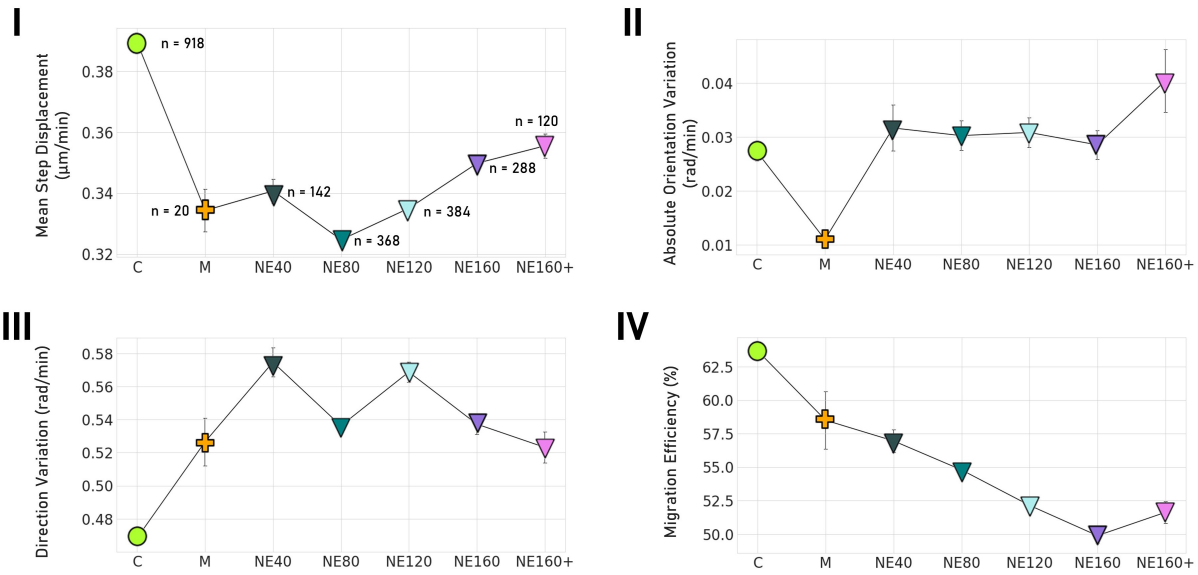

Figure 4.3: Distance-dependent analysis of migration features calculated. I) Mean step displacement (µm/min). II) Absolute orientation variation (rad/min). III) Direction variation (rad/min) and IV) Migration efficiency (%). n values indicated in I).

4.3 Nuclear morphology

Nuclear motion is seen to be impaired in the monolayer where stiffer nuclei are sparsely included. In order to understand the causes of this behaviour, or which other features could be correlated with the differences observed, it is interesting to first analyse nuclear morphology, as it is closely related with efficiency and coordination of the motion of the nucleus [57].

4.3.1 Morphometric feature analysis

Results regarding morphological features are presented in Figure 4.4. These reflect the average shape of the nucleus, described by numerical features often found to characterize shape.

M nuclei, due to the physiological consequences of the lamin A Del50 mutation, are expected to have a different aspect from normal or non-expressing cells [11]. Here, they are larger in size, but closer than NE nuclei to normal cells in terms of shape. Remarkably, NE nuclei are considerably different from both M and C cells, shape-wise. While the presence of M cells does not appear to impact NE nuclear area ($120.2 \pm 0.3929 \mu m^2$), which is similar to that of C ($122.3 \pm 0.5334 \mu m^2$), NE nuclei are considerably rounder (less eccentric) than both M and C nuclei. They are less concave than M nuclei, indicating that boundary irregularities may occur less or have smaller amplitude.

A more detailed description of the boundary shape and how this shape is changing over time may be provided by the morphological contour analysis, described below.

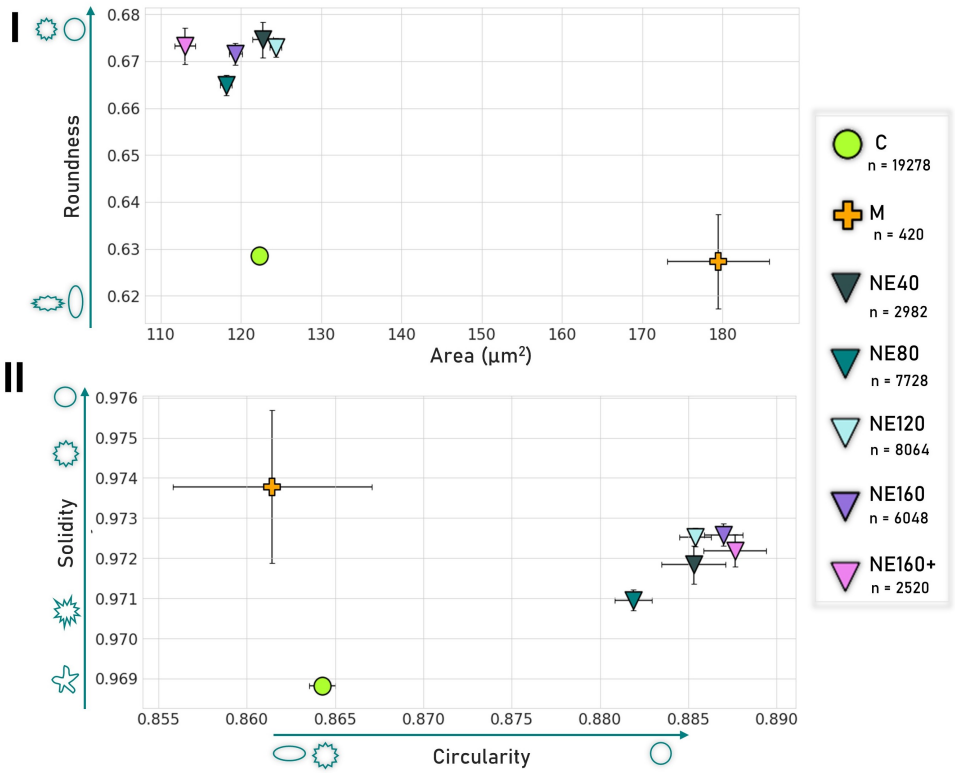

Figure 4.4: Distance-dependent analysis of static morphology features calculated. I) x-axis: Area (μm^2); y-axis: Roundness. II) x-axis: Circularity; y-axis: Solidity. Blue arrows and icons indicate shape differences according to the value of that features.

4.3.2 Spacial progression contour-based analysis

With the polar representation of the nuclear boundary, further insight may be provided into the average morphological characteristics of the nuclei of each group. Figure 4.5 displays a distance-dependent analysis of contour-based features which reflects spatial progression of the contour *i.e.* a detailed analysis from a static perspective.

Boundary irregularities seem to occur in larger amplitudes in C nuclei, when compared to both M and NE nuclei (Figure 4.5 I)). It is of note the growing tendency which can be observed in contour amplitude for the NE nuclei in a distance-dependent perspective, indicating that this particular effect of contour smoothing may decrease as distance to a mutant cell increases. For contour concavity (Figure 4.5 II)), M nuclei will not be commented due to the high heterogeneity of their phenotype. Few differences can be found between C and NE. These nuclei have similar values for contour concavity, indicating that this is not a discriminatory feature. Taken together, the results from this and the previous section indicate that C nuclei are more elongated and have a rougher boundary when compared to NE nuclei. Solidity is smaller for C nuclei, which is in line with the results for contour amplitude and abruptness (not shown), indicating that the amplitude of nuclear concavities is higher in a monolayer of normal cells,

when compared to the phenotype of NE nuclei.

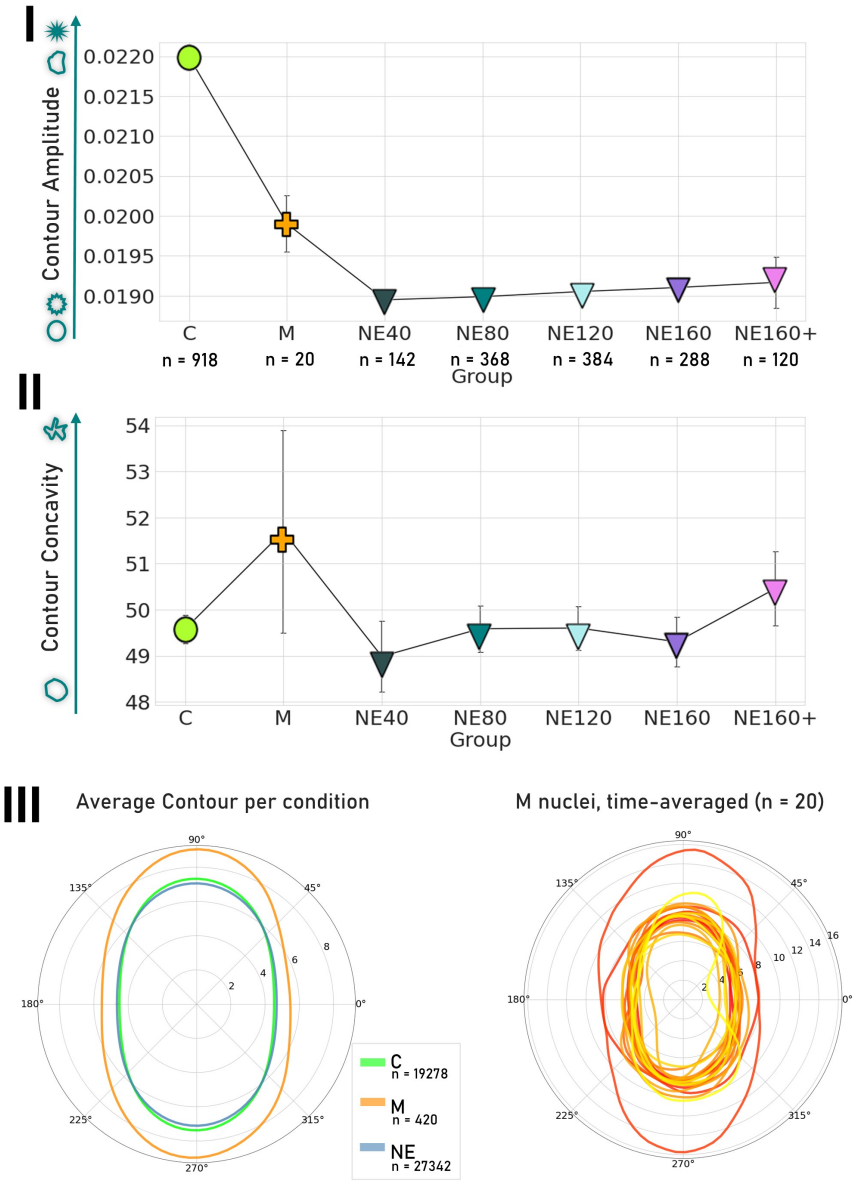

Figure 4.5: Distance-dependent analysis of static contour-based features calculated. I) Contour amplitude. II) Contour Concavity. III) Polar representation of the mean contour of each group (left) and of the time-averaged contour of each of the M nuclei (right). Different nuclei represented in curves in different shades of orange. Distances to the centroid in μm.

Figure 4.5 III) roughly illustrates the findings enumerated above. It depicts a representation of the *average nuclear shape*, by taking the time-average radii for each of the 100 contour points, for all the nuclei within the population of the groups under study (C, M, NE); of course, due to the large number of

cells included in the analysis, much contour detail is lost. In any case, while the area of C and NE nuclei is similar and smaller than that of M nuclei, NE nuclei do appear to be rounder than C nuclei. Note that, from the right figure in III), the representation of the time-averaged contour of all the M nuclei depicts one nucleus which is much larger than the remaining nuclei and very eccentric, which may be biasing the characterization of this group described above.

4.4 Nuclear dynamics, or temporal progression contour-based analysis

The results shown above hint that both morphology and migration of NE cells are affected by the presence of mutant, stiffer cells in the monolayer. A further insight could be provided by investigating if the nuclear membrane fluctuations, which determine shape alterations, are affected as well, which could reveal whether the flexibility of the nuclear envelope is maintained in NE nuclei or if these nuclei become unable to adjust to mechanical stimuli.

Figure 4.6 I) and II) shows that, as expected due to prior knowledge on the properties of HGPS cells [11], M nuclei have impaired morphological dynamics when compared to C cells, with significantly smaller amplitudes of temporal variation (*i.e.* due to the stiffness of their boundary, the "speed" by which the boundary changes is much smaller). Contrastingly, NE and C cells have very similar nuclear dynamics. Temporal abruptness (maximum radius variation from one frame to the other, or *how abruptly* the boundary can change) is not significantly different between both groups, indicating that the boundary stiffness is not altered in NE cells, and temporal contour amplitude (average radius variation between subsequent frames, or *how* the boundary fluctuates *on average*), while slightly inferior, is very close in average value.

The features shown reflect nuclear boundary averaged across time, but also across the boundary. A different analysis of nuclear dynamics can be performed without averaging temporal boundary variation across the spatial dimension, but rather only across time. For that, two metrics were defined, which are just variations of the calculation of temporal contour amplitude Δ_t (Table 3.3), but are a function of the spatial boundary m.

Relative temporal variation is calculated in a very similar way to the Δ_t, but it is not averaged across the boundary (Equation (4.1)):

$$\Delta_{t,rel}(m) = \frac{1}{N-1}\sum_{n}^{N-1} |\frac{r_{m,n+1} - r_{m,n}}{r_{m,n}}| \tag{4.1}$$

where n is one frame of $N = 21$ total frames, m is one boundary point of $M = 100$ boundary points, and $r_{m,n}$ is the distance to the nuclear centroid at that point (μm). Normalization, here, is necessary due

to differences in area in different groups (Figure 4.4 I)).

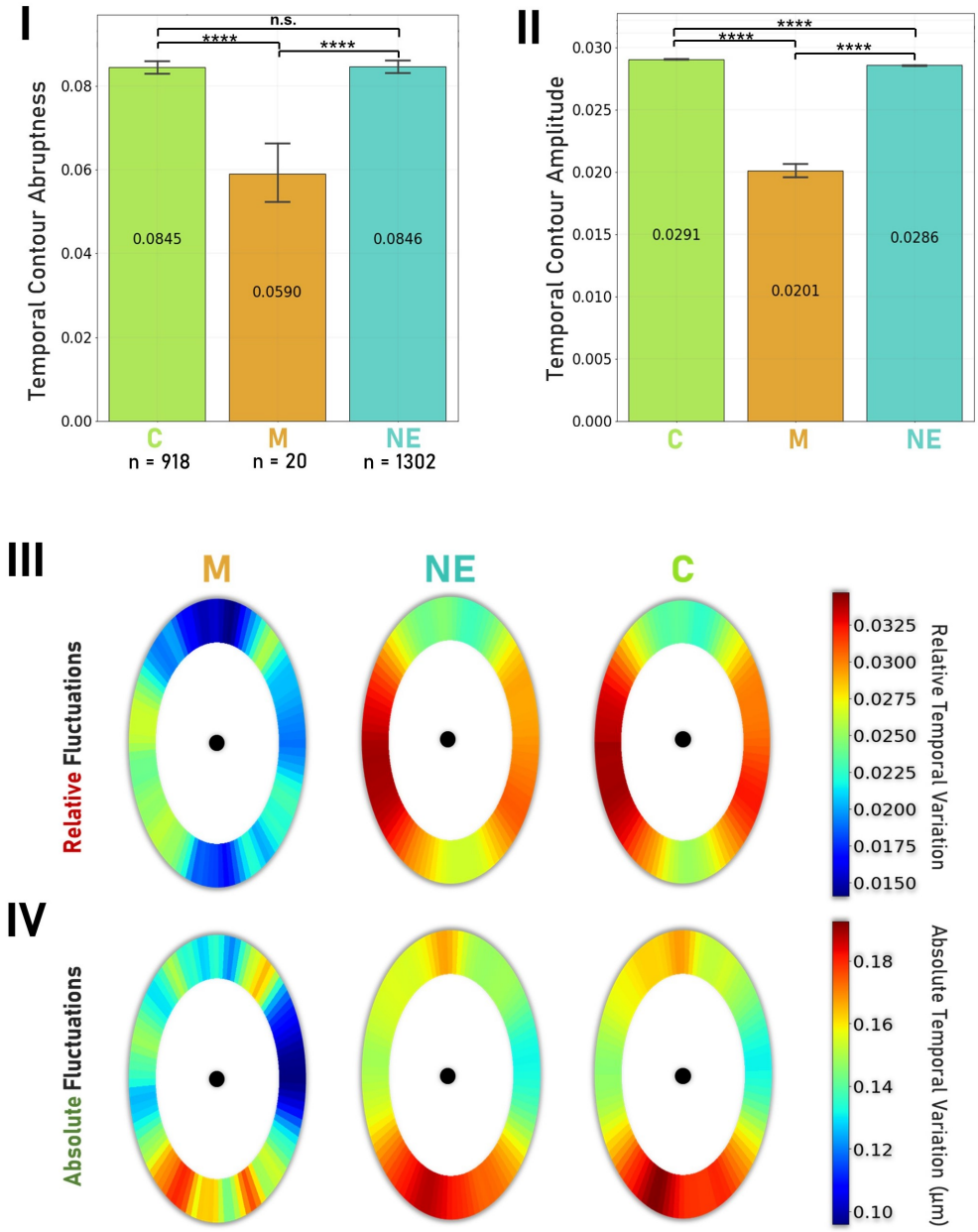

Figure 4.6: Group-based analysis of nuclear contour dynamics. I) Temporal contour abruptness. II) Temporal Contour Amplitude. Average value displayed on the bar. III) Average relative temporal variation, for different nuclei groups. Boundary points represented as oval shape. Magnitude (colour) reflects relative temporal variation. IV) Average absolute temporal variation (in μm), for different nuclei groups. Unpaired two-tailed t-test: $n.s. - p > 0.05; **** p \leq 0.0001$.

Conversely, to get a sense of the *absolute* variation, one obtains the average differences in boundary radius over time, in μm (Equation (4.2)).

$$\Delta_{t,abs}(m) = \frac{1}{N-1}\sum_{n}^{N-1} |r_{m,n+1} - r_{m,n}| \quad [\mu m] \tag{4.2}$$

For each nucleus, $\Delta_{t,rel}(m)$ and $\Delta_{t,abs}(m)$ are fully characterized by 100 datapoints (length of nuclear boundary). From this, one can obtain Figure 4.6 III) and IV), which reflect temporal progression over the spatial distribution of the boundary. Each nuclear shape represented (left to right, M, NE, C) corresponds to the average temporal variations for all nuclei of the respective group. Results as represented in oval shape to facilitate interpretation. Refer to Figure 3.4 for an illustration of nuclear boundary alignment. Figure A.3 contains an alternative representation the results in Figure 4.6 III) and IV).

Figure 4.6 III) indicates that the range of boundary variation is much smaller in M cells but similar in magnitude between C and NE nuclei. Furthermore, M nuclei have a much more heterogeneous distribution of nuclear membrane fluctuations. C and NE cells, however, have corresponding regions where the relative temporal variation of nuclear radius is quite homogeneous in magnitude. Note that the regions where this magnitude is higher correspond to regions where the radius is smaller (as described in Chapter 3, all the nuclei are aligned so that their major axis corresponds to the vertical direction; as such, the minor axis will the correspond to angles $\pm 180^{\circ}$ and 0°). Note that these results refer to radius variations which are *relative* to the absolute values of radii in the boundary ($\Delta r/r$). So, when r is smaller (as in the minor axis), the observed higher magnitudes of $\Delta_{t,rel}$ may actually correspond to similar variations (Δr) across the entire boundary.

In order to verify such hypothesis, $\Delta_{t,abs}(m)$, or absolute variation of boundary, is displayed in Figure 4.6 IV). While M cells continue to show a very spatially heterogeneous distribution of nuclear temporal variation, it appears to be more homogeneous across the boundary in C and NE nuclei, with the exception of boundary points near the $-\pi/2$ (-90°) region, where the major axis is defined. Such higher magnitudes of variation could be due to nuclear motion, with the major axis corresponding to the leading edge.

Another interesting analysis of nuclear boundary dynamics, though less detailed, can be performed by investigating how the numerical features calculated regarding nuclear morphology are changing over time. So, for feature F, feature variation is calculated as (Equation (4.3)):

$$\Delta_F(\%) = \frac{1}{N-1}\sum_{n}^{N-1} |\frac{F_{n+1} - F_n}{F_n}| \times 100 \tag{4.3}$$

where F_n is the value of feature F in time frame n. Figure 4.7 allows for a distance-dependent analysis of feature variation.

The heterogeneity in behaviour between different groups occurs in this case as well. In NE cells, area (I) appears to change less in the proximity of an M cell, although C nuclei-like variations can be seen as distance to a mutant cell increases. Nuclear eccentricity (II), in turn, varies more in NE cells

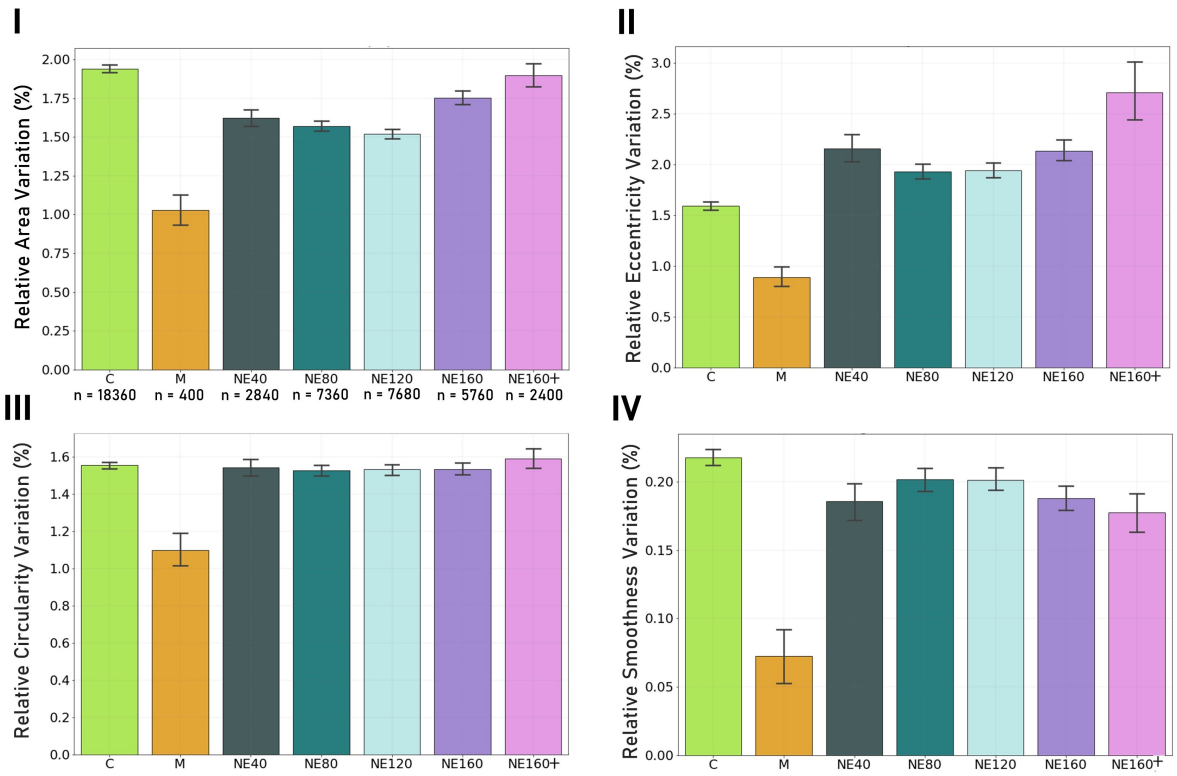

Figure 4.7: Distance-dependent analysis of dynamics of morphological features, in percentage of relative variation. I) Area. II) Eccentricity. III) Circularity. IV) Smoothness.

when compared to C cells, but the trend seen for increasing distance is similar to that of area.

Circularity (III), which relates shape and area-to-perimeter ratio, varies in a similar way in both C nuclei and all the groups of NE nuclei. When comparing these results with those for smoothness (IV), which measures perimeter irregularities, one can see that the trend observed for NE distance-dependent groups (increase followed by decrease in variation) is opposite to that of area (decrease followed by increase in variation). Because circularity relates these two variables, this could explain why the variations in circularity are so similar for C and NE nuclei across all the different subgroups. Again, what has been described points to a distance-dependent *compensatory dynamic behaviour* in NE cells. M nuclei, has would be expected, display inferior levels of variation of morphological indicators, due to the stiffness of the boundary.

Note that Figure 4.6 refers to the details of the dynamics and boundary mechanics by which nuclear shape is changing, but it does not reflect the net changes in nuclear morphology. Figure 4.7 complements this analysis by giving an overview of how these dynamics are affecting the overall shape of the nuclei.

4.5 Discussion

Regarding group sample distribution, which influences robustness of downstream analysis, one should mention the small number of samples composing the M cell group ($n = 20$), which amounts to less than 1% of the total number of nuclei analysed. The characterization of HGPS cells has been studied extensively [12, 58], and it was not the main focus of the present work, which intended to describe monolayer-level alterations stemming from the introduction of a small percentage of mechanodefective cells. Nonetheless, data for M nuclei was included in the results, providing a reference for the behaviour of these cells. Furthermore, one should note that the distance-dependent division of the NE cell group produces 5 groups of cells which have large number of samples but non-uniform distribution ($n_{min} = 120, n_{max} = 384$, see Table 4.1). Confidence intervals are in inverse proportion to group size, contributing to a critical analysis of the phenotype and behaviour observed.

A summary of the findings in this work is presented in Table 4.2. In addition to the data presented in Chapter 4, Appendix A.6 contains similar results for an alternative subgroup division of NE nuclei, which corroborates the main conclusions from the present work.

Table 4.2: Summary of findings for C and NE nuclei (rows) for each of the feature sets analysed (columns). Trends that mention *distance* refer to observed values of that feature for different subgroups with increasing distance to a mutant cell.

Feature / Nuclei	Nuclear Morphology	Nuclear Lamina Fluctuations	Nuclear Motion
C	• Elongated • Rough boundary	• Flexible nuclear boundary • Establishment of "leading edge", with ↑ lamina fluctuations	• Coordinated motion (↑ speed, ↓ direction changes) • High migration efficiency
NE	• Round • Smooth boundary (↓ with distance)	• Flexibility similar to C • "Leading edge" also observed	• Uncoordinated motion (↓ speed, ↑ direction changes) • Low migration efficiency (↓ with distance)
Distance-dependent effects in nuclear motion and fluctuations, as compensatory mechanism			

Regarding nuclear morphology, **NE nuclei are similar in size but more round than C nuclei**. These cells also have less concave nuclei (higher solidity).

Data for M nuclei, both due to their small sample size and to their heterogeneous appearance, were included in the analysis but interpreted carefully (see Figure 4.5 IV - one nucleus is significantly larger in size than the remaining nuclei of that group, which will certainly have an impact on the average value of morphometric features such as area). Overall, however, taking into account these factors, M nuclei analysed in the present study were larger, with similar shape to that of C nuclei (but more eccentric than NE nuclei) and with lamina irregularities which have higher amplitude than those of NE nuclei. Choi et

al. [12] describes these nuclei as smaller, more round and less solid, with a large number of small blebs. Goldman et al. [58], however, studies how the accumulation of mutant lamin A Del50 can influence nuclear shape and describes decreases in circularity with increased passage number, which result from perimeter increases (due to nuclear lobulation becoming more prominent) as well as an increase in area (although less pronounced than the perimeter increase, hence the observed decrease in circularity). The phenotype described in the present study would be consistent with the accumulation of the mutant lamin, but in order to take robust conclusions regarding the nuclear shape of M cells, the number of samples should be increased.

Philip and Dahl [4] shows that NE nuclei are more circular than C cells, which is in line with the findings described here. Regarding the analysis of the progression of the polar description of nuclear boundary, some interesting conclusions can be drawn. The growing trend of contour amplitude (equivalent to increasing roughness) observed for the NE subgroups indicates that this morphological adaptation of NE cells to the environment may depend on distance to a mechanically impaired cell. The values for this feature, however, are still significantly inferior to the contour amplitude of C cells, indicating that **smoother nuclei (lower contour amplitude) are a monolayer-level implication of the insertion of defective nuclei**. M nuclei appear have a higher value of contour concavity, which points to the existence of the nuclear lobulations, typical of this mutation.

Still regarding morphometric analysis, but considering the dynamics by which nuclear shape adjusts over time, **NE nuclei behave in a distance-dependent manner, and either preferably change shape/aspect ratio or smoothness/perimeter**, resulting in similar values of circularity variation for NE cells across the whole M+NE monolayer.

Interestingly, the mechanisms of nuclear membrane fluctuation do not appear to be affected in NE cells, while for M cells, due to increased nuclear stiffness, these nuclei are considerably less flexible. These results indicate that **while NE cells adapt through various mechanisms to the mechanical imbalances caused by the presence of M cells, membrane flexibility is not affected**. The calculation of the correlation between subsequent nuclear boundary curves, which can be seen in Figure A.4, further illustrates these findings.

Upon collective cell migration in a monolayer, the large-scale reorganization required is largely regulated by mechanisms of mechanical force sensing and response [59], where propagation of these signals is taking place through cell–cell junctions [16]. Mitosis and apoptosis events may cause perturbations to the dynamics of the monolayer, but the correlation between velocity vectors is usually high, indicating that a coordinated motion takes place. As was mentioned in Chapter 1, the nucleus and nuclear stiffness play an important role in cell migration [23], and HGPS cells migrate deficiently, which could be attributed to a decrease in nuclear deformability, decreased actin-myosin force generation [13], or inadequate establishment of cell polarization [31]. The formation of an actin-cap has been shown to be

fundamental for efficient nuclear motion [57] and in HGPS cells this component is often disorganized or absent [60], so impaired migration is to be expected.

Indeed, here, **a decrease in motion velocity and coordination can be observed for the M+NE monolayer**. Collective migration efficiency is significantly lower for NE nuclei, on average, and it appears to decrease with distance to the defect until a distance superior to 160μm from a mutant nucleus. This is a consequence of a lower net displacement to total distance ratio. Mean step displacement (motion velocity, a proxy for total distance) increases for a distance superior to 80 μm from a mutant nucleus, hinting that **the hindering of nuclear motion may be a short-range effect**. However, migration efficiency does not increase because net displacement (data now shown) does not increase, as a consequence of decreased coordination in collective cell migration. This implies that while the nuclei recover mobility potential when velocity starts increasing, their motion is still be impaired due to deficient force transmission or mechanoresponse from other neighbour NE cells, which is reflected in the poor coordination. It is important to note that net displacement reflects only the relation between initial and final positions, so it does not necessarily reflect the trend seen for either direction variation or absolute orientation variation, although these two features can be related to how coordinated cell motion is.

In a coordinated monolayer, cells will tend to elongate and align along preferential directions [59]. This would explain the average morphology observed for C nuclei, with NE cells having a rounder nucleus as a potential consequence of less defined direction of motion. In any case, it appears as though there is a preferential region for nuclear boundary changes in C and NE cells (Figure 4.6 IV)), indicating that monolayer dynamics and collective migration are dependent on the adjustment of the major axis of the nucleus and subsequent change in diameter along that direction. Cell polarization and nuclear rearward motion are to be expected in normal cells [23], and **the lack of an adequate nuclear arrangement which can be observed for M cells may be related to their reported inability to establish proper cell polarization [32]**.

In a stable monolayer, contractile and extensile forces are balanced [59]. Force imbalance may occur in normal monolayers as a consequence of misalignment points, locations with undefined local cell orientation axes (also called topological defects). For the M+NE monolayer, however, potentially due to abnormal force transmission by M cells, **these sites become sources of force imbalance, thus disturbing collective cell migration in neighbouring areas**.

The aforementioned study by Philip et al. [4] had observed the attenuation of response to shear stress in NE cells, but the cause of this behaviour is unclear. Curiously, lamin reorganization and upregulation in NE cells appears to be impaired to a greater degree than both control and mutant lamin A Del50 cells. Cell-cell signaling (gene expression is affected in HGPS cells [61]) or the alteration of the flow patterns of the monolayer (due to the connection between lamins and the cytoskeleton, which is deficient in HGPS cells [11]) could be at the origin of the findings in this and in the present work.

Overall, collective cell migration is impaired in the M+NE monolayer and trajectories are more scattered and disordered due to higher changes in direction and slightly higher rotation speeds. From the nuclear lamina fluctuations observed, it appears that NE nuclei maintain the ability to adjust to mechanical stimuli; as such, what is causing the differences in nuclear shape and motion could be related to abnormal internal force generation and transmission in the M+NE monolayer (an interesting analysis of the discriminatory features for C and NE nuclei can be seen in Figure A.5). Nevertheless, due to the large number of factors which are altered in HGPS cells and due to the complexity of cell-cell interactions, it is yet unclear which are the underlying causes for the phenotype observed and what is the ”chain of events” leading to the morphological and behavioural differences described above.

5

Concluding remarks and future work

Contents

5.1 Conclusion

The work presented here provides methods for the analysis and complete description of nuclear behaviour in a monolayer. A large array of techniques for image analysis and processing were used, in an attempt to objectively quantify phenotypic differences.

The conceptualization and extraction of features from the nuclear boundary provides a better understanding of shape and dynamics of nuclei, with great potential for elucidating how nuclear morphology evolves and adjusts to the environment. While the full analysis involved the calculation of a set of features larger than that presented here, only those deemed more significant were kept for analysis, mostly due to redundancy.

The main challenges in performing an analysis such as this relate to both the extraction of segmentation masks and appropriate tracking, which is inevitably a potential source of error or bias, and the translation of numeric, quantitative features into concrete, qualitative phenotype. However, by using the same methods across all preparations to achieve the first task, with minimal manual input, any potential bias is propagated throughout the entire dataset and thus differences found between groups should not be a consequence of the pipeline used for segmentation and tracking.

Tracking nuclear position and maintaining identity has allowed for a dynamic study of shape evolution and nuclear motion. Because both dimensions are interdependent - nuclear motion depends on adaptation of nuclear shape and migration depends on nuclear lamina fluctuations - a better portrait of mechanoresponse and nuclear behaviour can be obtained. Indeed, we note that both migration and morphology are affected in normal cells by the presence of M nuclei. Velocity of nuclear motion is inferior across the monolayer, when compared to a monolayer of normal cells. The shape of NE nuclei is rounder, which could be causing the decreased velocity or could be caused by the decreased motion coordination (*i.e.* because direction of migration varies, nuclear shape does not align with preferred directions of motion). While membrane fluctuation potential points to nuclear flexibility not being affected by the presence of M cells, previous studies [4] had noted that lamin reorganization is impaired in NE cells, which could be leading to the inhibition of nuclear eccentricity and having consequences at a migration level. Distance-dependency of some of the effects observed indicates that neighbouring cells sense a mechanical imbalance and try to compensate by exhibiting abnormal behaviour which then propagates throughout the monolayer.

By laying a basis for the understanding on nuclear behaviour in conditions of abnormal force transmission, the present work consists of yet another step in the direction of finding the principles which govern cell and tissue biomechanics, including the complex mechanisms of cellular behaviour, sensing, and interaction of internal and external stimuli. Downstream applications may include the study of mechanisms of disease onset and dissemination, with the development of better therapeutic alternatives.

5.2 Future Work

The present analysis could be expanded to reveal the mechanisms underlying the phenotype observed and the extent of the influence of mechanically impaired cells - topological defects - in a monolayer.

Because of the microscopy amplification used and the density of M cells in the M+NE monolayer, one cannot evaluate the total range of the effect of one isolated defect in a monolayer of normal cells. Some of the differences found in the present work could fade as distance to a stiff nucleus increases, but for this analysis the density of mutant cells did not allow such conclusions to be taken.

In line with such studies, varying the density of M cells in the monolayer could also shed light on the mechanisms governing the behavioural changes observed. The present work analysed a monolayer with a roughly estimated density of M cells of 10%, and this was sufficient to produce generalized differences between the M+NE and the control settings. What would be the effect of an isolated M cell, both in the behaviour of this cell and its neighbours, and what could be the range of influence? Do the values of some features scale proportionally to the density of M cells (*e.g.* would migration be further debilitated and uncoordinated, would morphology become more radically different)?

It could also be interesting to analyse how morphological features and motion features correlate, by performing a cross-correlation analysis of the temporal evolution of nuclear shape and trajectories. Nuclear morphology and cell migration have been proven to be correlated [57], but such relation may not be found in M or NE nuclei due to impaired mechanoresponse.

A more complete characterization of the cellular response of NE cells to the presence of M cells could be achieved by staining and tracking other elements of the cell. Nuclear description could include a quantification of chromatin distribution and condensation within the nucleus. This is yet another component of the cell which is intimately related with mechanotransduction and could be at the origin of the phenotype observed [20]. Tracking of chromatin could also be included in the analysis.

Staining of the lamins, namely lamin A, could also give insight into the mechanisms controlling cellular response, due to the influence of this component on nuclear stiffness. Finally, by staining the cell membrane, conclusions could be drawn from the relative positioning of the nucleus in the cell (which influences cell migration) and from the strength of cell-cell junctions, involved in force transmission and monolayer integrity.

Force transmission and nuclear stiffness could also be investigated by using techniques like Atomic Force Microscopy (AFM).

Finally, a 3D analysis could be performed to provide a new perspective on mechanoresponse in a tissue and how cells interact to compensate for topological defects.

Bibliography

[1] R. Eils and C. Athale, “Computational imaging in cell biology,” *Journal of Cell Biology*, vol. 161, no. 3, pp. 477–481, 2003.

[2] B. Preim and D. Bartz, *Visualization in Medicine: Theory, Algorithms, and Applications*. San Francisco, CA, USA: Morgan Kaufmann Publishers Inc., 2007.

[3] D. Zink, A. H. Fischer, and J. A. Nickerson, “Nuclear structure in cancer cells,” *Nature Reviews Cancer*, vol. 4, no. 9, pp. 677–687, 2004.

[4] J. T. Philip and K. N. Dahl, “Nuclear mechanotransduction: Response of the lamina to extracellular stress with implications in aging,” *Journal of Biomechanics*, vol. 41, no. 15, pp. 3164–3170, 2008.

[5] M. H. Lee, P. H. Wu, J. R. Staunton, R. Ros, G. D. Longmore, and D. Wirtz, “Mismatch in mechanical and adhesive properties induces pulsating cancer cell migration in epithelial monolayer,” *Biophysical Journal*, vol. 102, no. 12, pp. 2731–2741, 2012. [Online]. Available: http://dx.doi.org/10.1016/j.bpj.2012.05.005

[6] M. Stiekema, M. A. van Zandvoort, F. C. Ramaekers, and J. L. Broers, “Structural and Mechanical Aberrations of the Nuclear Lamina in Disease,” *Cells*, vol. 9, no. 8, 2020.

[7] K. Piekarowicz, M. Machowska, V. Dzianisava, and R. Rzepecki, “Hutchinson-Gilford Progeria Syndrome—Current Status and Prospects for Gene Therapy Treatment,” *Cells*, vol. 8, no. 2, p. 88, 2019.

[8] K. N. Dahl, A. J. Ribeiro, and J. Lammerding, “Nuclear shape, mechanics, and mechanotransduction,” *Circulation Research*, vol. 102, no. 11, pp. 1307–1318, 2008.

[9] N. Belaadi, J. Aureille, and C. Guilluy, “Under Pressure: Mechanical Stress Management in the Nucleus,” *Cells*, vol. 5, no. 2, p. 27, 2016.

[10] T. Harada *et al.*, “Nuclear lamin stiffness is a barrier to 3D migration, but softness can limit survival,” *Journal of Cell Biology*, vol. 204, no. 5, pp. 669–682, 2014.

[11] K. N. Dahl, P. Scaffidi, M. F. Islam, A. G. Yodh, K. L. Wilson, and T. Misteli, “Distinct structural and mechanical properties of the nuclear lamina in Hutchinson-Gilford progeria syndrome,” *Proceedings of the National Academy of Sciences of the United States of America*, vol. 103, no. 27, pp. 10 271–10 276, 2006.

[12] S. Choi *et al.*, “Computational image analysis of nuclear morphology associated with various nuclear-specific aging disorders,” *Nucleus*, vol. 2, no. 6, pp. 570–579, 2011.

[13] E. A. Booth-Gauthier, V. Du, M. Ghibaudo, A. D. Rape, K. N. Dahl, and B. Ladoux, “Hutchinson-Gilford progeria syndrome alters nuclear shape and reduces cell motility in three dimensional model substrates,” *Integrative Biology (United Kingdom)*, vol. 5, no. 3, pp. 569–577, 2013.

[14] M. T. Parreira, K. Lavrenyuk, J. M. Sanches, and K. Dahl, “Stiffened nuclei reduce persistent movement between cells in a monolayer but motor forces are conserved as cell fluctuations,” 2021, to be submitted.

[15] D. Jaalouk and J. Lammerding, “Mechanotransduction gone awry,” *Nature reviews. Molecular cell biology*, vol. 10, pp. 63–73, 02 2009.

[16] X. Serra-Picamal *et al.*, “Mechanical waves during tissue expansion,” *Nature Physics*, vol. 8, no. 8, pp. 628–634, 2012. [Online]. Available: http://dx.doi.org/10.1038/nphys2355

[17] J. Swift *et al.*, “Nuclear lamin-A scales with tissue stiffness and enhances matrix-directed differentiation,” *Science*, vol. 341, no. 6149, pp. 1358–1375, 2013.

[18] A. L. McGregor, C. R. Hsia, and J. Lammerding, “Squish and squeeze - the nucleus as a physical barrier during migration in confined environments,” *Current Opinion in Cell Biology*, vol. 40, pp. 32–40, 2016. [Online]. Available: http://dx.doi.org/10.1016/j.ceb.2016.01.011

[19] K. N. Dahl, E. A. Booth-Gauthier, and B. Ladoux, “In the middle of it all: Mutual mechanical regulation between the nucleus and the cytoskeleton,” *Journal of Biomechanics*, vol. 43, no. 1, pp. 2–8, 2010.

[20] E. A. Booth, S. T. Spagnol, T. A. Alcoser, and K. N. Dahl, “Nuclear stiffening and chromatin softening with progerin expression leads to an attenuated nuclear response to force,” *Soft Matter*, vol. 11, pp. 6412–6418, 2015. [Online]. Available: http://dx.doi.org/10.1039/C5SM00521C

[21] A. Athirasala, N. Hirsch, and A. Buxboim, “Nuclear mechanotransduction: sensing the force from within,” *Current Opinion in Cell Biology*, vol. 46, pp. 119–127, 2017. [Online]. Available: http://dx.doi.org/10.1016/j.ceb.2017.04.004

[22] J. Lammerding, “Mechanics of the nucleus,” *Comprehensive Physiology*, vol. 1, no. 2, pp. 783–807, 2011.

[23] F. J. Calero-Cuenca, C. S. Janota, and E. R. Gomes, “Dealing with the nucleus during cell migration,” *Current Opinion in Cell Biology*, vol. 50, pp. 35–41, 2018.

[24] F. Houben *et al.*, “Disturbed nuclear orientation and cellular migration in A-type lamin deficient cells,” *Biochimica et Biophysica Acta - Molecular Cell Research*, vol. 1793, no. 2, pp. 312–324, 2009. [Online]. Available: http://dx.doi.org/10.1016/j.bbamcr.2008.10.003

[25] J. Löber, F. Ziebert, and I. S. Aranson, “Collisions of deformable cells lead to collective migration,” *Scientific Reports*, vol. 5, pp. 1–7, 2015.

[26] R. Alert and X. Trepat, “Physical Models of Collective Cell Migration,” *Annual Review of Condensed Matter Physics*, vol. 11, pp. 77–101, 2020.

[27] D. M. Graham *et al.*, “Enucleated cells reveal differential roles of the nucleus in cell migration, polarity, and mechanotransduction,” *Journal of Cell Biology*, vol. 217, no. 3, pp. 895–914, 2018.

[28] C. J. Hutchison, “Do lamins influence disease progression in cancer?” *Advances in Experimental Medicine and Biology*, vol. 773, pp. 593–604, 2014.

[29] K. Manju, B. Muralikrishna, and V. K. Parnaik, “Expression of disease-causing lamin A mutants impairs the formation of DNA repair foci,” *Journal of Cell Science*, vol. 119, no. 13, pp. 2704–2714, 2006.

[30] A. D. Stephens *et al.*, “Physicochemical mechanotransduction alters nuclear shape and mechanics via heterochromatin formation,” *Molecular Biology of the Cell*, vol. 30, no. 17, pp. 2320–2330, 2019.

[31] C. Östlund, W. Chang, G. G. Gundersen, and H. J. Worman, “Pathogenic mutations in genes encoding nuclear envelope proteins and defective nucleocytoplasmic connections,” *Experimental Biology and Medicine*, vol. 244, no. 15, pp. 1333–1344, 2019.

[32] W. Chang, Y. Wang, G. W. G. Luxton, C. Östlund, H. J. Worman, and G. G. Gundersen, “Imbalanced nucleocytoskeletal connections create common polarity defects in progeria and physiological aging,” *Proceedings of the National Academy of Sciences*, vol. 116, no. 9, pp. 3578–3583, 2019. [Online]. Available: https://www.pnas.org/content/116/9/3578

[33] B. T. Grys, D. S. Lo, N. Sahin, O. Z. Kraus, Q. Morris, C. Boone, and B. J. Andrews, “Machine learning and computer vision approaches for phenotypic profiling,” *Journal of Cell Biology*, vol. 216, no. 1, pp. 65–71, 12 2016. [Online]. Available: https://doi.org/10.1083/jcb.201610026

[34] V. Wiesmann, D. Franz, C. Held, C. Münzenmayer, R. Palmisano, and T. Wittenberg, “Review of free software tools for image analysis of fluorescence cell micrographs,” *Journal of microscopy*, vol. 257, 10 2014.

[35] J. Schindelin *et al.*, “Fiji: An open-source platform for biological-image analysis,” *Nature methods*, vol. 9, pp. 676–82, 06 2012.

[36] C. McQuin *et al.*, “Cellprofiler 3.0: Next-generation image processing for biology,” *PLOS Biology*, vol. 16, no. 7, pp. 1–17, 07 2018. [Online]. Available: https://doi.org/10.1371/journal.pbio.2005970

[37] F. Chaumont *et al.*, “Icy: an open bioimage informatics platform for extended reproducible research,” *Nature methods*, vol. 9, pp. 690–6, 07 2012.

[38] N. Otsu, “A threshold selection method from gray-level histograms,” *IEEE Transactions on Systems, Man, and Cybernetics*, vol. 9, no. 1, pp. 62–66, 1979.

[39] L. Vincent and P. Soille, “Watersheds in digital spaces: an efficient algorithm based on immersion simulations,” *IEEE Transactions on Pattern Analysis and Machine Intelligence*, vol. 13, no. 6, pp. 583–598, 1991.

[40] M. Kass, A. Witkin, and D. Terzopoulos, “Snakes: Active contour models,” *International Journal of Computer Vision*, vol. 1, no. 4, pp. 321–331, 1988.

[41] A. A. Dima *et al.*, “Comparison of segmentation algorithms for fluorescence microscopy images of cells,” *Cytometry Part A*, vol. 79A, no. 7, pp. 545–559, 2011. [Online]. Available: https://onlinelibrary.wiley.com/doi/abs/10.1002/cyto.a.21079

[42] M. Maška *et al.*, “A benchmark for comparison of cell tracking algorithms,” *Bioinformatics*, vol. 30, no. 11, pp. 1609–1617, 02 2014. [Online]. Available: https://doi.org/10.1093/bioinformatics/btu080

[43] K. E. Magnusson, J. Jalden, P. M. Gilbert, and H. M. Blau, “Global linking of cell tracks using the viterbi algorithm,” *IEEE Transactions on Medical Imaging*, vol. 34, no. 4, pp. 911–929, 2015.

[44] A. Dufour, R. Thibeaux, E. Labruyere, N. Guillen, and J. Olivo-Marin, “3-D Active Meshes: Fast Discrete Deformable Models for Cell Tracking in 3-D Time-Lapse Microscopy,” *IEEE Transactions on Image Processing*, vol. 20, no. 7, pp. 1925–1937, 2011.

[45] J.-Y. Tinevez *et al.*, “Trackmate: An open and extensible platform for single-particle tracking,” *Methods*, vol. 115, pp. 80 – 90, 2017, image Processing for Biologists. [Online]. Available: http://www.sciencedirect.com/science/article/pii/S1046202316303346

[46] A. Kan, “Machine learning applications in cell image analysis,” *Immunology & Cell Biology*, vol. 95, no. 6, pp. 525–530, 2017. [Online]. Available: https://onlinelibrary.wiley.com/doi/abs/10.1038/icb.2017.16

[47] O. Ronneberger, P. Fischer, and T. Brox, “U-net: Convolutional networks for biomedical image segmentation,” *Lecture Notes in Computer Science (including subseries Lecture Notes in Artificial Intelligence and Lecture Notes in Bioinformatics)*, vol. 9351, pp. 234–241, 2015.

[48] J. C. Caicedo *et al.*, “Evaluation of deep learning strategies for nucleus segmentation in fluorescence images,” *Cytometry Part A*, vol. 95, no. 9, pp. 952–965, 2019. [Online]. Available: https://onlinelibrary.wiley.com/doi/abs/10.1002/cyto.a.23863

[49] E. C. Filippi-Chiela, M. M. Oliveira, B. Jurkovski, S. M. Callegari-Jacques, V. D. da Silva, and G. Lenz, “Nuclear morphometric analysis (NMA): Screening of senescence, apoptosis and nuclear irregularities,” *PLoS ONE*, vol. 7, no. 8, 2012.

[50] A. Medyukhina, M. Blickensdorf, Z. Cseresnyés, N. Ruef, J. V. Stein, and M. T. Figge, “Dynamic spherical harmonics approach for shape classification of migrating cells,” *Scientific Reports*, vol. 10, no. 1, pp. 1–12, 2020.

[51] F. C. Crow, “Summed-area tables for texture mapping,” *SIGGRAPH Comput. Graph.*, vol. 18, no. 3, p. 207–212, Jan. 1984. [Online]. Available: https://doi.org/10.1145/964965.808600

[52] H. Bay, A. Ess, T. Tuytelaars, and L. Van Gool, “Speeded-up robust features (surf),” *Computer Vision and Image Understanding*, vol. 110, no. 3, pp. 346 – 359, 2008, similarity Matching in Computer Vision and Multimedia. [Online]. Available: http://www.sciencedirect.com/science/article/pii/S1077314207001555

[53] A. Dufour, V. Meas-Yedid, A. Grassart, and J.-C. Olivo-Marin, “Automated quantification of cell endocytosis using active contours and wavelets,” *Proceedings - International Conference on Pattern Recognition*, no. May 2014, 2008.

[54] C. Monzel and K. Sengupta, “Measuring shape fluctuations in biological membranes,” *Journal of Physics D: Applied Physics*, vol. 49, no. 24, 2016.

[55] M. Hubert and S. Van der Veeken, “Outlier detection for skewed data,” *Journal of Chemometrics*, vol. 22, no. 3[U+2010]4, pp. 235–246, 2008. [Online]. Available: https://onlinelibrary.wiley.com/doi/abs/10.1002/cem.1123

[56] S. M. Ross, “Chapter 7 - parameter estimation,” in *Introduction to Probability and Statistics for Engineers and Scientists (Fifth Edition)*, fifth edition ed., S. M. Ross, Ed. Boston: Academic

Press, 2014, pp. 235 – 296. [Online]. Available: http://www.sciencedirect.com/science/article/pii/B9780123948113500071

[57] D. H. Kim, S. Cho, and D. Wirtz, "Tight coupling between nucleus and cell migration through the perinuclear actin cap," *Journal of Cell Science*, vol. 127, no. 11, pp. 2528–2541, 2014.

[58] R. D. Goldman *et al.*, "Accumulation of mutant lamin A progressive changes in nuclear architecture in Hutchinson-Gilford progeria syndrome," *Proceedings of the National Academy of Sciences of the United States of America*, vol. 101, no. 24, pp. 8963–8968, 2004.

[59] T. Chen, T. B. Saw, R. M. Mege, and B. Ladoux, "Mechanical forces in cell monolayers," *Journal of Cell Science*, vol. 131, no. 24, 2018.

[60] S. B. Khatau *et al.*, "A perinuclear actin cap regulates nuclear shape," *Proceedings of the National Academy of Sciences*, vol. 106, no. 45, pp. 19 017–19 022, 2009. [Online]. Available: https://www.pnas.org/content/106/45/19017

[61] J. Lammerding *et al.*, "Lamin A/C deficiency causes defective nuclear mechanics and mechanotransduction," *Journal of Clinical Investigation*, vol. 113, no. 3, pp. 370–378, 2004.

A

Supplementary Material

A.1 Numerical Averages and Statistical Significance

The following tables (Table A.2, Table A.3, Table A.4, Table A.5, Table A.6, Table A.7) contain the numerical averages and respective confidence intervals for all the data shown in Chapter 4. Differences between the control condition and other groups are tested for statistical significance using a two-tailed unpaired t-test, and the p-value is reflected in the colouring of the cell, according to Table A.1. Colour reflects how the average value of that feature compares between that group and the control group (green if greater than C, red if lesser than C) and the tone reflects statistical significance.

Table A.1: Colour to p-value correspondence, used to represent statistical significance and average value evolution. Green is used to represent groups whose average is greater than that of the control condition, and red represents groups with smaller average.

$>$ **C (**$p > 0.05$**)**	$>$ **C (**$0.01 < p \leq 0.05$**)**	$>$ **C (**$p \leq 0.01$**)**	$<$ **C (**$p > 0.05$**)**	$<$ **C (**$0.01 < p \leq 0.05$**)**	$<$ **C (**$p \leq 0.01$**)**

Table A.2: Average value and 95% CI for Figure 4.2.

Group	Normalized Net Displacement	CV of direction of motion
C	0.3097 ± 0.008864	0.7323 ± 0.1208
Del50A	0.2166 ± 0.008091	
Del50B	0.239 ± 0.01239	
NE		1.683 ± 0.5139

Table A.3: Average value and 95% CI for Figure 4.3.

Group	Mean Step Displacement (μm/min)	Absolute Orientation Variation (rad/min)	Direction Variation (rad/min)	Migration Efficiency (%)
C	0.3894 ± 0.001315	0.02728 ± 0.00163	0.4684 ± 0.002419	63.68 ± 0.2756
M	0.3343 ± 0.006984	0.01095 ± 0.0009742	0.5265 ± 0.01443	58.5 ± 2.137
NE40	0.3407 ± 0.003957	0.03168 ± 0.004275	0.5747 ± 0.008887	56.96 ± 0.8409
NE80	0.3247 ± 0.002154	0.03026 ± 0.00275	0.5362 ± 0.004236	54.79 ± 0.5178
NE120	0.3351 ± 0.001985	0.03085 ± 0.00274	0.5688 ± 0.005974	52.14 ± 0.4854
NE160	0.3498 ± 0.002624	0.02854 ± 0.002701	0.5373 ± 0.006019	49.88 ± 0.5547
NE160+	0.3555 ± 0.003992	0.04046 ± 0.005862	0.5232 ± 0.009274	51.62 ± 0.8166

Table A.4: Average value and 95% CI for Figure 4.4.

Group	Area (μm^2)	Roundness	Circularity	Solidity
C	122.3 ± 0.5334	0.6285 ± 0.001331	0.8643 ± 0.0007447	0.9688 ± 0.0002025
M	179.4 ± 6.326	0.6273 ± 0.01003	0.8614 ± 0.005638	0.9738 ± 0.001912
NE40	122.7 ± 1.284	0.6746 ± 0.003795	0.8853 ± 0.001817	0.9718 ± 0.0004766
NE80	118.1 ± 0.6991	0.6649 ± 0.002165	0.8819 ± 0.00106	0.971 ± 0.000262
NE120	124.3 ± 0.7179	0.6729 ± 0.001974	0.8854 ± 0.0008996	0.9725 ± 0.0002297
NE160	119.3 ± 0.8528	0.6716 ± 0.002274	0.8870 ± 0.001108	0.9726 ± 0.0002784
NE160+	113.0 ± 1.27	0.6732 ± 0.00388	0.8876 ± 0.001769	0.9722 ± 0.0003981

Table A.5: Average value and 95% CI for Figure 4.5 and Figure A.4.

Group	Contour Amplitude	Contour Abruptness	Contour Concavity	Mean Cross-Correlation
C	$0.02199 \pm 2.083 \times 10^{-5}$	0.06172 ± 0.00181	49.58 ± 0.3127	3570.0 ± 74.14
M	$0.0199 \pm 3.547 \times 10^{-4}$	0.06677 ± 0.0218	51.7 ± 2.199	5325.0 ± 916.6
NE40	$0.01895 \pm 1.037 \times 10^{-4}$	0.05296 ± 0.003646	48.99 ± 0.7685	3587.0 ± 178.8
NE80	$0.01899 \pm 6.721 \times 10^{-5}$	0.05461 ± 0.002138	49.59 ± 0.5015	3446.0 ± 97.32
NE120	$0.01905 \pm 4.539 \times 10^{-5}$	0.05175 ± 0.001867	49.6 ± 0.4738	3638.0 ± 100.1
NE160	$0.0191 \pm 7.381 \times 10^{-5}$	0.05211 ± 0.002306	49.3 ± 0.5429	3485.0 ± 118.6
NE160+	$0.01917 \pm 3.209 \times 10^{-4}$	0.05351 ± 0.003236	50.46 ± 0.8105	3289.0 ± 176.4

Table A.6: Average value and 95% CI for Figure 4.6.

Group	Temporal Contour Abruptness	Temporal Contour Amplitude
C	0.08448 ± 0.001533	0.02909 ± 0.00002774
M	0.05903 ± 0.007521	0.02011 ± 0.0005585
NE	0.08461 ± 0.001478	0.02861 ± 0.00003246

Table A.7: Average value and 95% CI for Figure 4.7.

Group	Area Variation (%)	Eccentricity Variation (%)	Circularity Variation (%)	Smoothness Variation (%)
C	1.941 ± 0.02473	1.59 ± 0.03997	1.554 ± 0.0185	0.2179 ± 0.0059
M	1.028 ± 0.09503	0.8891 ± 0.09405	1.099 ± 0.08726	0.07262 ± 0.01982
NE40	1.625 ± 0.05494	2.157 ± 0.1336	1.541 ± 0.0449	0.186 ± 0.01325
NE80	1.572 ± 0.03494	1.931 ± 0.07423	1.527 ± 0.02824	0.2017 ± 0.008736
NE120	1.521 ± 0.03191	1.941 ± 0.07156	1.531 ± 0.02853	0.2014 ± 0.008783
NE160	1.754 ± 0.04332	2.133 ± 0.1043	1.534 ± 0.0322	0.1879 ± 0.009156
NE160+	1.899 ± 0.0755	2.704 ± 0.2954	1.591 ± 0.05161	0.1775 ± 0.01386

A.2 Nuclear Boundary Interpolation

In order to perform the contour-based analysis, all the nuclear boundaries (21 for each nucleus) were interpolated into 100 datapoints, as is explained in Chapter 3. This allows contours to be easily compared and a large set of features to be calculated. However, interpolation may be poorly implemented and lead to loss of information. As such, different methods of interpolation were compared using Mean Squared Error (MSE), which calculates the differences between the original datapoints $r(m)$ and the corresponding values in the interpolated contour $r_i(m)$ for all M points of each nuclear boundary (Equation (A.1)):

$$MSE = \frac{1}{M}\sum_{m}^{M} e(m)^2 = \frac{1}{M}\sum_{m}^{M}(r_i(m) - r(m))^2 \tag{A.1}$$

The results for the different groups of nuclei, for a cubic, quadratic and linear spline interpolation can be seen in Figure A.1. Cubic spline interpolation was used, as the error was minimum.

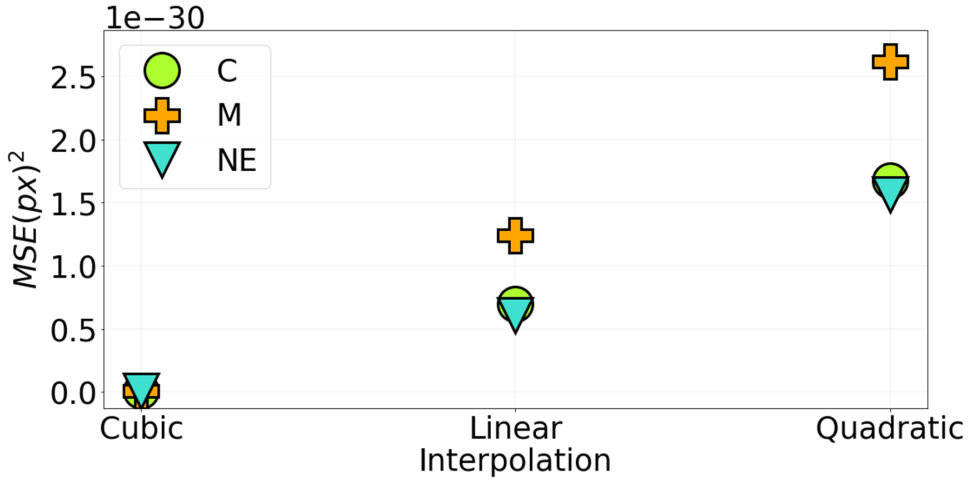

Figure A.1: MSE for different interpolation methods (cubic, linear, quadratic) and different nuclei groups. Data for r_m in px, representing distances to the nuclear centroid.

A.3 Monolayer Dynamics

The calculation of the time-averaged Mean Square Displacement (MSD) can further illustrate differences in collective cell migration across the two conditions studied. Taking the position of the centroid on each nucleus i at time t, $p = (x_t^i, y_t^i)$, time-averaged MSD is calculated as can been seen in Equation (A.2):

$$MSD_i(\tau) =< \Delta p^i(\tau)^2 >=< (x_{t+\tau}^i - x_t^i)^2 + (y_{t+\tau}^i - y_t^i)^2 > \tag{A.2}$$

where $<>$ represents a time-average over t and τ stands for lag time. The values of MSD obtained

for each group (Figure A.2) are the result of averaging the MSD(τ) for each value of τ.

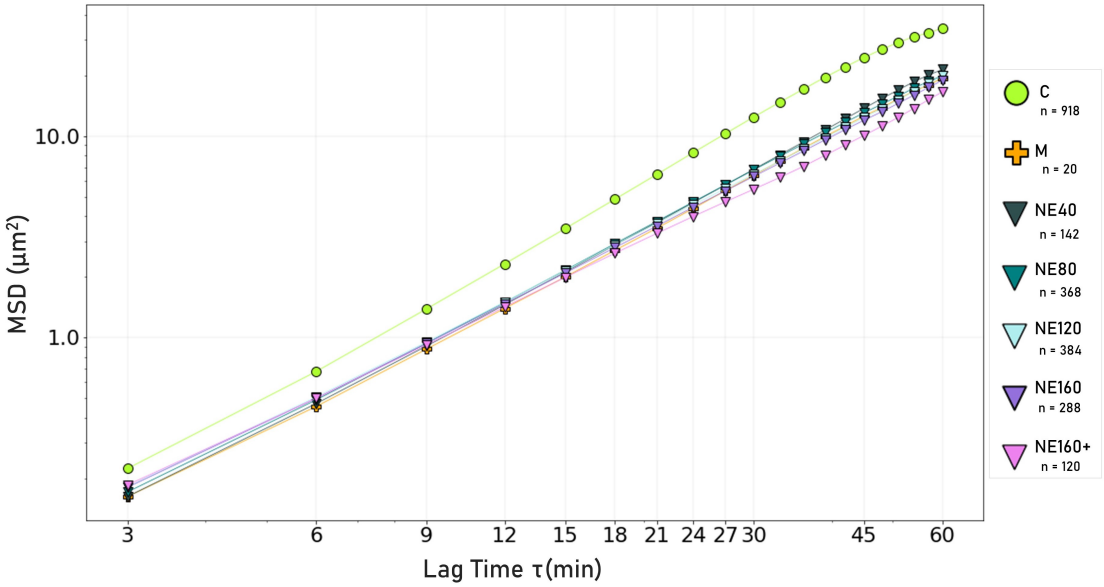

Figure A.2: Time-averaged mean square displacement across groups. x-axis: lag time (τ), in minutes. y-axis: MSD(τ), in μm^2. Both axis shown in logarithmic scale.

The decreased mean square displacement is observed across all subgroups in the M+NE monolayer, much like what had been seen in Chapter 4. Collective cell migration is impaired by the presence of progeria-like cells.

A.4 Dynamic contour-based analysis

The two sections below are concerned with the dynamic analysis of nuclear lamina fluctuations, providing alternative forms of interpreting data from the present analysis.

A.4.1 Nuclear membrane fluctuations

The data from Figure 4.6 III) and IV) is presented in a ring-like shape to facilitate interpretation of contour variation. Here, those results are displayed as a two-dimensional plot, which may assist their interpretation (Figure A.3). The same conclusions can be drawn: the profile of nuclear membrane fluctuations is very similar between C and NE nuclei, and of noticeable inferior magnitude for M nuclei.

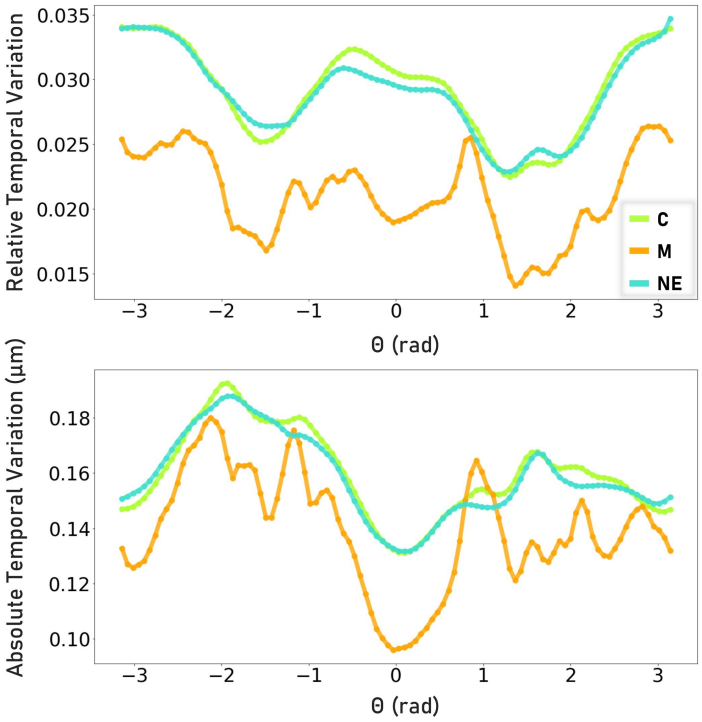

Figure A.3: Relative (top) and Absolute (bottom) temporal variation, as a function of boundary position (θ, in radians), for all groups of interest (C, M and NE).

A.4.2 Temporal cross-correlation

In addition to the data regarding the temporal variation of the polar representation of contours, additional features can be calculated to give a sense of nuclear shape variation, namely similarity features such as cross-correlation, euclidean distances or cosine distances. In order to further illustrate the results of Chapter 4 regarding nuclear lamina fluctuations, one can calculate temporal cross-correlation in a nucleus (Equation (A.3)). Let $r_n(m)$ be a vector corresponding to the nuclear boundary in frame n ($m \in [1, 100]$). Cross-correlation γ can be calculated as:

$$\gamma(k) = (r_{n+1} \star r_n)(k) = \sum_m \overline{r_{n+1}(m)} r_n(m+k) \tag{A.3}$$

Where $\overline{r_{n+1}(m)}$ is the complex conjugate of $r_{n+1}(m)$. Because $r_n(m)$ corresponds to a "spatial series", not a time series, cross-correlation was analysed only at the point of maximum overlap (zero lag, $k = 0$). So, each nucleus is defined by 20 values of temporal cross-correlation, which can be averaged to give a sense of how much nuclear boundary is changing in subsequent time frames (Figure A.4).

In line with what could be observed for Figure 4.6, the temporal variation of the nuclear boundary is more significant for C and NE nuclei than for M nuclei (note that cross-correlation measures *similarity*,

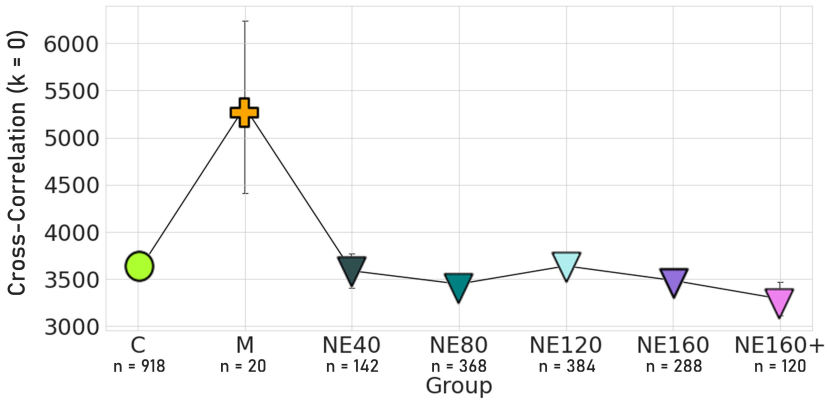

Figure A.4: Mean cross-correlation at displacement $k = 0$, across groups.

whereas temporal contour abruptness and amplitude measure *differences* between subsequent nuclear boundaries), and it is very similar for C and NE nuclei, further supporting the idea that, while nuclear shape may be different, the mechanisms by which shape fluctuates remain unchanged.

A.5 Feature Selection

In order to understand how features are related and how nuclear boundary dynamics could be translated through a distribution of data points in the feature space, a Principal Component Analysis (PCA) was performed. This is a very popular linear method for dimension reduction, but it may also be used for exploratory data analysis. It results in a set of orthogonal basis vectors (each a Principal Component (PC)), ordered by explained variance and representing directions of progressively smaller variance [2]. It can also be used for data visualization, by projecting all the multi-dimensional data points into a 2D plot where the two first PCs are represented. By analysing which features correlate the most with these two directions, one can get insight into how features relate and which could be used as discriminatory features across groups of analysis (C and NE, particularly).

Contour-based features (from the polar representation of the nuclear boundary) have the particularity of allowing the study of both spatial and temporal evolution of the contour. Seven numerical features have been described in Table 3.3, and the projection of the 7-dimensional data from C and NE nuclei ($n = 2020$) in the first two PCs (cumulative explained variance of 59.4%) can be seen in Figure A.5.

Two clusters are readily observable, each regarding one group of nuclei. When contemplating the distribution of the projection of datapoints in each PC axis, the first principal component (PC1) shows almost no overlap (good separation of groups) whereas PC2 shows significant overlap between distributions. Table A.8 displays the correlation between each one of the features considered and the two first PCs. It can be seen that the first PC has higher magnitude projections over features which relate

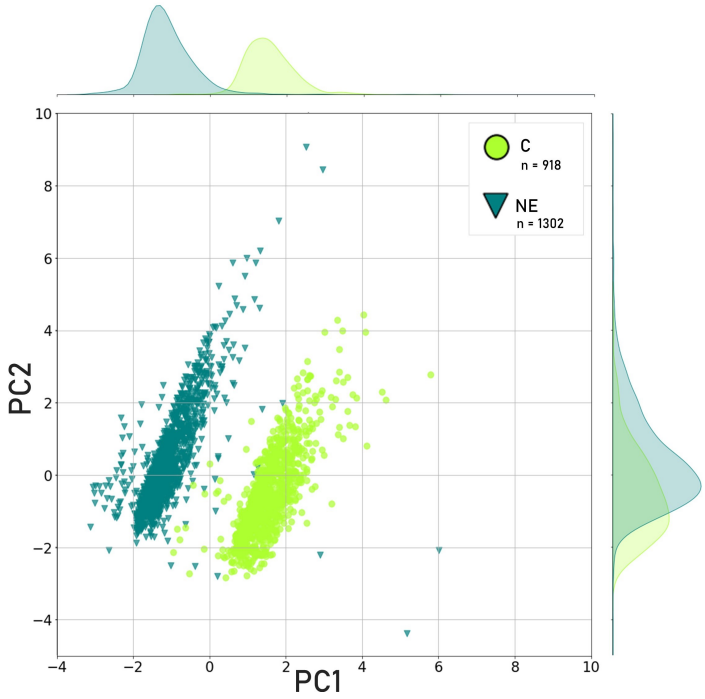

Figure A.5: Projection of C and NE nuclei datapoints in a 2D plane formed by the first two PCs. Curves representing the projected distribution of points on each axis are plotted on top (PC1) and right (PC2) of the figure.

to spatial progression of the contour (contour range and contour amplitude) whereas PC2 has higher magnitude in the direction of temporal progression related features (temporal contour range and temporal contour abruptness). In Figure 4.5 and Figure 4.6 it can be seen that, while nuclear boundary aspect differs between C and NE nuclei, nuclear lamina fluctuation is not greatly affected by the presence of M nuclei. Data visualization using PCA provides an alternative analysis which reflects analogous findings, where spatial variation can be seen as a discrimination criteria, but temporal progression of the nuclear boundary is similar between both groups.

Table A.8: Direction of the two first principal components in each of the contour-based features. Highlighted in green are the two features whose projection of that PC is maximum.

PC	Contour Concavity	Contour Range	Contour Amplitude	Contour Abruptness	Temporal Contour Range	Temporal Contour Amplitude	Temporal Contour Abruptness
1	0.0049	0.5933	0.5966	0.2673	0.2396	0.3463	0.2078
2	-0.0055	-0.2624	-0.2623	0.1437	0.6414	-0.0457	0.6542

A.6 Distance-dependency in alternative subgroup division

All the results thus far presented in this work, in which the distance to an M nucleus is taken into account to form different subgroups of NE nuclei, are based on a 40 μm radius difference. Figure A.6 and Figure A.7 illustrate results similar to those in Figure 4.3, Figure 4.5 and Figure 4.7 but for a 25μm radius difference (NE25 includes nuclei whose centroid distance to an M nucleus, d, is $d \leq 25\mu$m; NE50 is for nuclei with $25 < d \leq 50\mu$m, etc.). This analysis can reveal differences in behaviour at a slightly smaller scale, and help understand the compensatory/counter-compensatory mechanism that the results in Chapter 4 appear to suggest.

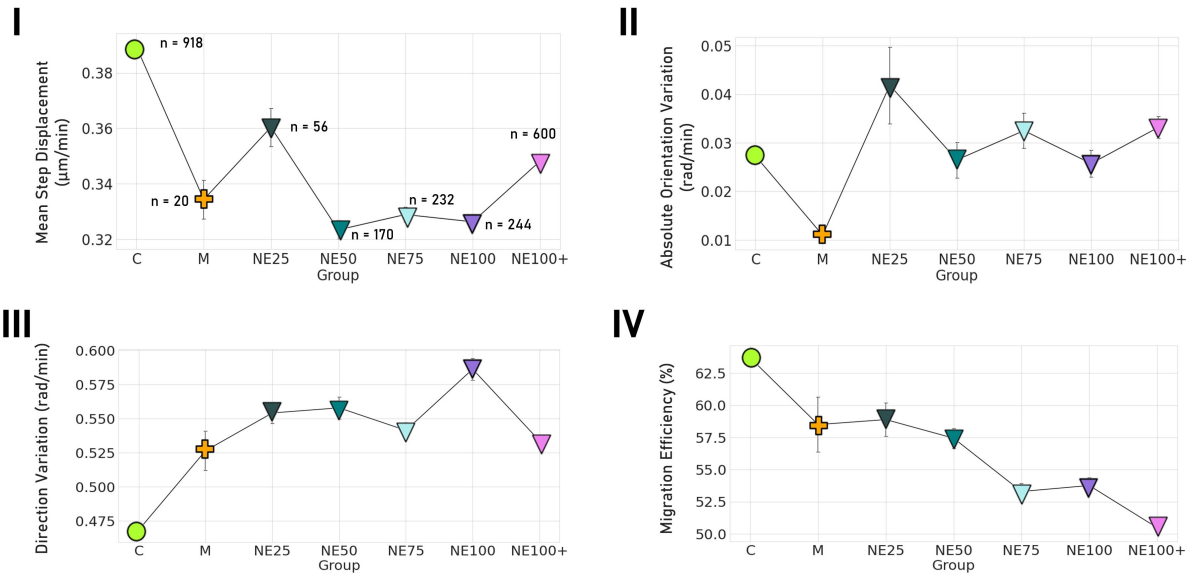

Figure A.6: Distance-dependent analysis of migration features calculated. I) Mean step displacement (μm/min). II) Absolute orientation variation (rad/min). III) Direction variation (rad/min) and IV) Migration efficiency (%). n values indicated in I).

The behaviour of the nuclei closest to M nuclei becomes more evident as a compensation mechanism for the disruption of force transmission and mechanical sensing caused by M cells. This can be seen in nuclear motion, by higher velocity of translation and rotation, as well as in changes in eccentricity. The compensatory/counter-compensatory behaviour which appears to emerge from this monolayer imbalance is confirmed and particularly evident for mean step displacement (velocity) and direction variation, as well as area variation. The decrease in motion efficiency and increase in abruptness of the contour (contour amplitude) with distance can still be observed, even at this smaller scale for subgroup division, confirming that these features have a mostly monotonous progression in relation to distance to a mechanical defect.

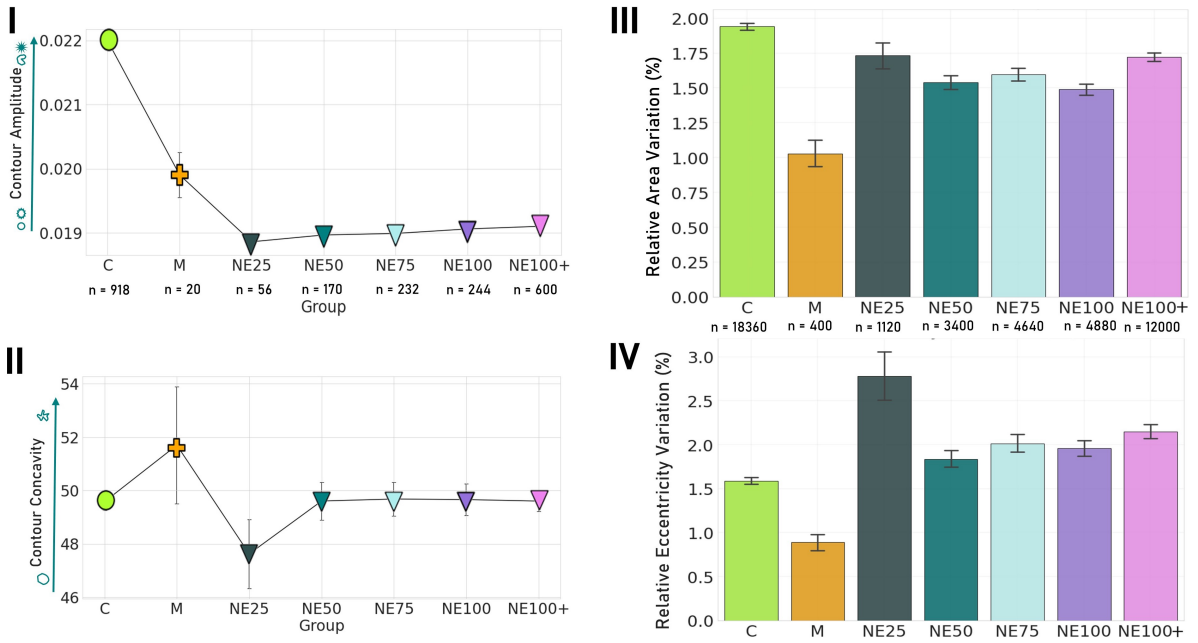

Figure A.7: Distance-dependent analysis of static contour-based features calculated (I and II) and of dynamics of morphological features, in percentage of relative variation(III and IV). I) Contour amplitude. II) Contour Abruptness. III) Area (%). IV) Eccentricity (%). n values indicated in I) and III).